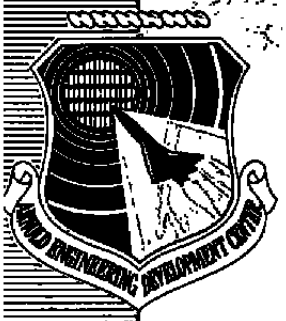

New Particle Diagnostic Methods in Arc-Heated Ablation/Erosion Facilities

D. B. Brayton, B. W. Bomar, P. D. Elrod,
and B. L. Seiber
ARO, Inc.

August 1981

Final Report for Period October 1, 1976 – September 30, 1980

ARNOLD ENGINEERING DEVELOPMENT CENTER
ARNOLD AIR FORCE STATION, TENNESSEE
AIR FORCE SYSTEMS COMMAND
UNITED STATES AIR FORCE

NOTICES
When U. S. Government drawings, specifications, or other data are used for any purpose other than a definitely related Government procurement operation, the Government thereby incurs no responsibility nor any obligation whatsoever, and the fact that the Government may have formulated, furnished, or in any way supplied the said drawings, specifications, or other data, is not to be regarded by implication or otherwise, or in any manner licensing the holder or any other person or corporation, or conveying any rights or permission to manufacture, use, or sell any patented invention that may in any way be related thereto.
Qualified users may obtain copies of this report from the Defense Technical Information Center.
References to named commercial products in this report are not to be considered in any sense as an indorsement of the product by the United States Air Force or the Government.

This report has been reviewed by the Office of Public Affairs (PA) and is releasable to the National Technical Information Service (NTIS). At NTIS, it will be available to the general public, including foreign nations.

APPROVAL STATEMENT

This report has been reviewed and approved.

Marshall K. Kingery

MARSHALL K. KINGERY
Directorate of Technology
Deputy for Operations

Approved for publication:

FOR THE COMMANDER

Marion L. Laster

MARION L. LASTER
Director of Technology
Deputy for Operations

REPORT DOCUMENTATION PAGE		READ INSTRUCTIONS BEFORE COMPLETING FORM
1 REPORT NUMBER AEDC-TR-80-64	2. GOVT ACCESSION NO.	3 RECIPIENT'S CATALOG NUMBER
4 TITLE (and Subtitle) NEW PARTICLE DIAGNOSTIC METHODS IN ARC-HEATED ABLATION/EROSION FACILITIES		5 TYPE OF REPORT & PERIOD COVERED Final Report - Oct. 1, 1976 - Sept. 30, 1980 6. PERFORMING ORG REPORT NUMBER
7. AUTHOR(s) D. B. Brayton, B. W. Bomar, P. D. Elrod, and B. L. Seiber, ARO, Inc., a Sverdrup Corporation Company		8 CONTRACT OR GRANT NUMBER(s)
9 PERFORMING ORGANIZATION NAME AND ADDRESS Arnold Engineering Development Center/DOT Air Force Systems Command Arnold Air Force Station, TN 37389		10. PROGRAM ELEMENT, PROJECT, TASK AREA & WORK UNIT NUMBERS Program Element 65807F
11 CONTROLLING OFFICE NAME AND ADDRESS Arnold Engineering Development Center/DOS Air Force Systems Command Arnold Air Force Station, TN 37389		12. REPORT DATE August 1981 13. NUMBER OF PAGES 73
14 MONITORING AGENCY NAME & ADDRESS(if different from Controlling Office)		15 SECURITY CLASS. (of this report) UNCLASSIFIED 15a DECLASSIFICATION/DOWNGRADING SCHEDULE N/A

16 DISTRIBUTION STATEMENT (of this Report)

Approved for public release; distribution unlimited.

17 DISTRIBUTION STATEMENT (of the abstract entered in Block 20, if different from Report)

18 SUPPLEMENTARY NOTES

Available in Defense Technical Information Center (DTIC).

19 KEY WORDS (Continue on reverse side if necessary and identify by block number)

arc heating	lasers	orthogonality
particles	thermal radiation	test facilities
ablation	chemiluminescence	test methods
erosion	particle flux	nose cones
photodetectors	electrooptics	computer applications

20 ABSTRACT (Continue on reverse side if necessary and identify by block number)

Arc-heated flow facilities with injected particles are used at the Arnold Engineering Development Center (AEDC) to simulate the erosive and ablative/erosive environments encountered by spacecraft reentry through fog, clouds, thermonuclear explosions, etc. Newly developed electro-optical particle diagnostic techniques used to calibrate these facilities are discussed. Each of these techniques acquires data by optically probing the in-flight particle field. One technique measures particle velocity and is based on the detec-

DD FORM 1 JAN 73 1473 EDITION OF 1 NOV 65 IS OBSOLETE

20. ABSTRACT, Concluded.

tion of thermal radiation and/or chemiluminescence from the hot seed particles in a model ablation/erosion facility. A second technique measures a localized rate per unit area or mass flux of particles in a dust erosion tunnel (DET) facility; this technique is based on the photodetection of singular events caused by particles intercepting a laser beam. The third technique, similar to the latter, employs a multilaser beam arrangement to measure the velocity, two orthogonal dimensions of size, and the relative contribution of rate per unit area of individual, in-flight particles in the DET facility.

AFSC
Arnold AFS Tenn

PREFACE

The research reported herein was performed by the Arnold Engineering Development Center (AEDC), Air Force Systems Command (AFSC). Work and analysis for this research were done by personnel of ARO, Inc., AEDC Group, (a Sverdrup Corporation Company), operating contractor of the AEDC, AFSC, Arnold Air Force Station, Tennessee. The work covered the period from October 1, 1976 to September 30, 1980 and was done under Project Number P32N-40. Mr. M. K. Kingery was the Air Force project manager. The manuscript was submitted for publication on October 21, 1980.

Mr. H. R. Bevis, ARO, Inc., not only assisted, but also contributed significantly to all phases of development effort. His outstanding effort is acknowledged and appreciated.

Messrs. Brayton, Bomar, Elrod, and Seiber are currently employed by Calspan Field Services, Inc., AEDC Division.

CONTENTS

ILLUSTRATIONS

Figure — Page

Figure | Page

APPENDIXES

1.0 INTRODUCTION

Arc-heated particle-injected (seeded) flow facilities are used at Arnold Engineering Development Center (AEDC) to test nose cone materials and geometries by simulating the erosive and ablative/erosive environments of spacecraft reentry. The two high enthalpy ablation testing (HEAT) facilities at AEDC each employ a seeded arc jet exiting into a low expansion ratio nozzle with relatively high static pressure (1 atm) to generate a high-velocity (1,500 $msec^{-1}$), high-temperature (2,000 to 4,000°K), and high number density (a few particles per cm^3) dust cloud entrained in hot (2,000 to 5,000°K) gas that produces model erosion and ablation. The Dust Erosion Tunnel (DET) facility at AEDC employs a seeded arc jet exiting into a high expansion ratio nozzle with low static pressure (much less than 1 atm) to generate a high-velocity (1,000 to 3,000 $msec^{-1}$), low-temperature (a few hundred °K), and low number density (1,000 to 2,000 per m^3) dust cloud entrained in a low-density, cool exit gas that causes model erosion.

These facilities must be calibrated for particle field characteristics. To this end, newly developed calibration instruments are described. One, the thermal emission velocimeter (TEV) measures the velocity of high-temperature particles in the HEAT facilities. Individual particle velocities are measured by collecting and photodetecting light self-radiated by a particle crossing two small, spatially separated, and separately photodetected regions in the flow. The two photodetected pulses then gate an electronic counter, thereby measuring the time interval between pulses and providing the time versus distance measurement of velocity. Data are sequentially recorded to provide a time history of particle velocity at a point. A second instrument, the particle rate monitor (RM), monitors the relative changes in local particle rate, which is proportional to local particle mass flux in the DET facility. The rate monitor photodetects interruptions or blockages of a single laser beam as individual particles pass through the beam near its focus. Individual photodetected events are counted over fixed time intervals and recorded, thereby monitoring relative particle rate. A third technique, called the laser multibeam technique, measures a velocity component, two orthogonal dimensions of size, and the relative rate per unit area contribution of individual, inflight particles that pass through a local detection region. Many laser beams, in a special geometrical arrangement, are separately photodetected. The multiple photodetected signals resulting from a single particle passing through these beams are electronically processed and recorded. Many such records provide size, velocity, and relative rate per unit area contribution of individual particle detections. The multiple laser beams, each of special geometry, converge to small cross-sectional dimensions and separational distances in the detection region that approximate the mean particle size to be detected.

Particle diagnostic measurements using the TEV and the rate monitor techniques have been developed to the point that they are now effective, reliable diagnostic tools. The laser multibeam technique, currently in a prototype development stage, has been applied to demonstrate the feasibility.

The remainder of this report is concerned with the design and application of these instruments to the HEAT and DET facilities.

2.0 PARTICLE DIAGNOSTICS IN THE HEAT FACILITIES

As previously mentioned, the HEAT facilities produce both an ablative and an erosive testing environment. Gas temperature and velocity are nominally 2,000 to 5,000°K and 1,000 to 2,000 $msec^{-1}$, respectively, and the small injected particles of nominally 100- to 200-μm-diam carbon material are heated, ablated, and accelerated in the nozzle to temperatures, sizes, and velocities that are generally unknown until measured.

Streak photography using a high-speed camera, laser velocimetry, pulsed laser holography (Ref. 1) and thermal emission velocimetry (Ref. 2) have all been applied to measure the dust cloud parameters of the HEAT facilities. Photographing the hot particles with a high-speed camera produced streak image recordings from which particle velocity could be measured with ± 15 to ± 20 percent accuracy; such a technique has been used over the entire range of the facility operating conditions. A laser velocimeter (LV) that used four interference fringes, a 30-deg off-axis, backward- scattering angle, a high-power argon-ion laser, and a narrow bandwidth spectral filter produced good signals at low working gas temperatures (up to 2,700°K). However, very little particle velocity data could be recorded, as signal processing/recording instrumentation applicable to low cycle count LV signals was not then available. However, such an LV potentially can provide ± 10 percent accurate velocity data over all HEAT facility operating conditions if proper signal processing and narrower bandwidth spectral filtering are employed. The pulsed laser holographic recording technique, (Ref. 1) using the HEAT arc jet as an optical diffuser and recording holograms on the jet far side, produced reconstructed particle images of marginal quality. More recently, the thermal emission velocimeter (TEV) technique (Ref. 2) measured particle velocity through essentially the entire operating range of the HEAT facilities and with ± 5 percent accuracy. The TEV was much simpler to build, operate, and maintain in comparison to the proposed LV system and produced similar results. It is now thought that the TEV technique can be expanded or a multiple laser beam technique (similar to the DET applied multiple laser beam technique discussed herein) can be developed to permit total particle field parameter measurements in the HEAT facility in the near future; such an effort is currently underway at AEDC.

3.0 THERMAL EMISSION VELOCIMETER SYSTEM

The TEV principles of operation and its specific design and application to DET will now be presented. Also to be discussed will be general design considerations that affect the TEV system performance.

3.1 TEV OPERATING PRINCIPLES

The TEV measures the velocity of hot particles by detecting the thermal radiation emitted by a particle when its trajectory carries it through each of two spatially separated probe volumes.

The TEV detection system shown in Fig. 1 defines two regions or volumes in space, V1 and V2, that (1) are regions of maximum light collection and detection efficiency (Appendix A discusses light collection efficiency) and (2) are spatially separated by a known distance. That is, the electro-optical detection systems to the left in Fig. 1 will detect a point source of light with high relative collection efficiency only when it lies within one of the two detection regions V1 and V2. Thus, a hot particle moving along the z axis in Fig. 1 through these regions while emitting thermal radiation will generate photodetected signal amplitudes versus particle spatial position as indicated in Fig. 2. Knowledge of the spatial distance between the two detection volumes and the transit time between the two signal maxima permits a calculation of particle velocity.

Throughout the remainder of this report it will be assumed, unless otherwise stated, that the probe volumes and/or the particle number density are sufficiently small such that only one particle at a time is detected.

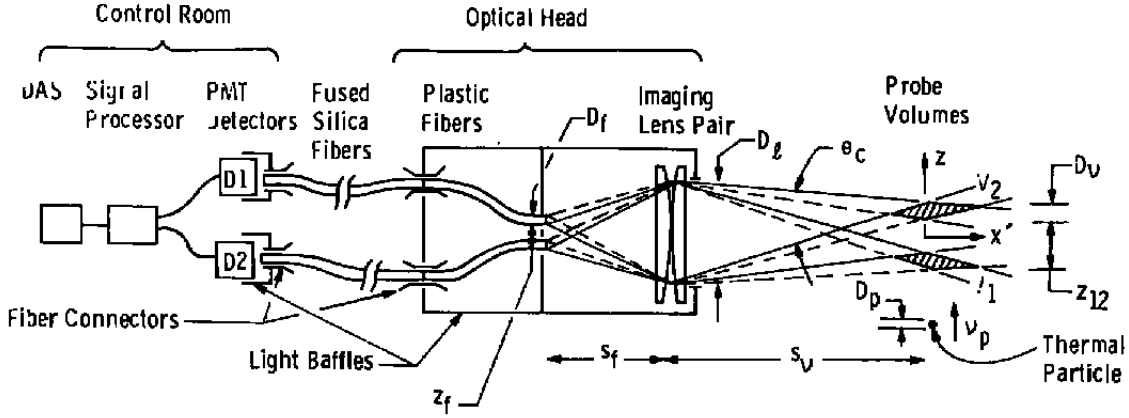

Figure 1. Thermal emission velocimeter.

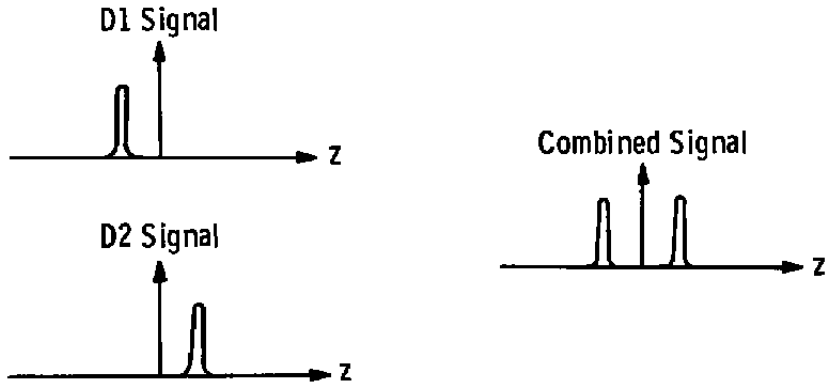

Figure 2. Detected signal amplitudes versus particle position.

3.2 TEV OPTICAL DESIGN

The most common TEV optical design employed at the AEDC is illustrated in Fig. 1, with an exception that many times only one photomultiplier tube (PMT) detector is employed to detect both optical signals (with both fiber-optic components directed to the common PMT). Two achromatic collimating lenses were employed back-to-back to first collect and collimate the radiated signals, and then to focus the collimated signals onto the ends of two optical fibers. The fiber ends served as limiting apertures. The fiber optics collected the signals and transmitted them to the control room where they were photodetected. Plastic fibers were used in the detector head where short radius bends were required, and glass fibers of high transmission efficiency transmitted the signals to the detector(s). All of the fiber-optic components were single, continuous elements of 250-μm diameter. The high noise level of arc current-induced electromagnetic radiation emitted by the HEAT facilities suggested that the photodetectors and other electronic instrumentation be located in the shielded environment of the control room, located 30 m from the arc heater.

The wavelength selectivity of the optical system components caused the overall system radiation detection efficiency to be very low; nevertheless, it was adequate for detection purposes. Even though the transmission bandwidth of the lenses and optical fibers of nominally 400 to 1,100 nm approximately coincided with the peak of the spectral emission band of the thermal radiation from the nominally 2,000 to 4,000°K particle, (see Appendix A), the thermal emission bandwidth was approximately a factor of 4 larger than the transmission bandwidth of the optics. Furthermore, the bandwidth of the PMT detectors employed (which were existing detectors and not specially selected for the application) was very narrow (320 to 530 nm) and further reduced the optical system effective bandwidth by an additional factor of 8. Wide bandwidth PMT detectors are generally available with gallium arsenide photocathode material that have high responsivity over a 240- to 880-nm bandwidth.

3.3 TEV PROBE VOLUME GEOMETRY

The TEV probe volume geometry can be varied by changing the configuration of the collecting optics. Specific probe volume geometries that affect TEV performance will now be discussed.

The three-dimensional geometry of the probe volume can be scaled up or down by changing the diameter of the virtual aperture, D_v, through the equation $D_v = s_v s_f^{-1} D_f$, where the quantities in this equation are defined in Fig. 1 and in Appendix A. If conventional spherical surface lenses are used with a circular aperture in axial symmetry, then for $s_v >> D_f >> D_v$ (Fig. 1) the volume of the principal or high collection efficiency region of the probe volume (the shaded region of Fig. 1) is

$$V_v \cong \frac{\pi D_v^3}{6 \theta_c} \tag{1}$$

A TEV optical design that provides both the smallest probe region maximum or length dimension and minimal systematic measurement error is shown in Fig. 3. Note that the probe volumes are not totally in line along the flow direction. Time periods would be measured as particles traversed between the two probe volumes, as with the normal TEV. However, at the signal period $\tau = D_v v_p^{-1}$ signal data would accumlate above the baseline data because of particles intercepting both probe volumes, thereby generating effective probe volumes of much smaller maximum dimension. The maximum length of the effective probe volumes is given by (see Fig. 3)

$$L_v = \frac{D_v}{\sin\left[(\theta_{1,2} + \theta_v)/2\right]} \tag{2}$$

Note also that the probe volume centerlines are both parallel to the $x'-y$ plane; therefore, the normal (though usually small) systematic error associated with a nonuniform distance between the probe volumes is eliminated.

The concept that a relatively simple optical system consisting of an imaging lens system and the single opening of an aperture will collect point source radiation with high efficiency from only a small, definable region in space is fundamental to the design of a TEV and is outlined in Appendix B. Statement 2 of Appendix B, which identifies which rays will be collected, can be used to describe the probe volume geometry using collection efficiency

contours. For the case of a circular aperture stop at the optical fibers and a circular lens system aperture stop, the single probe volume collection efficiency contours are x-axis symmetric as indicated in Fig. 4a, which contains xz and xy plane two-dimensional plots of contours of constant radiation collection efficiency.

Two important probe volume geometries result when either one of the single probe volume aperture stops is changed from a circle to a narrow slit, as illustrated in Figs. 4b and c. Both are important to TEV design since they can be advantageously used as follows: (1) a reduction in the z-axis width of the aperture of the imaging lens system reduces the single probe volume signal duration for remote (or noncentral) particle trajectories to correspond to $\Delta z \cong D_p + D_v$ particle displacement* (see Fig. 4b with particle trajectory parallel to the z-axis); (2) a reduction in the z-axis width of the aperture of the optical fiber reduces the single probe volume signal duration for central particle trajectories to correspond to $\Delta z \cong D_p$ particle displacement, assuming $\Delta z_v << D_p$.

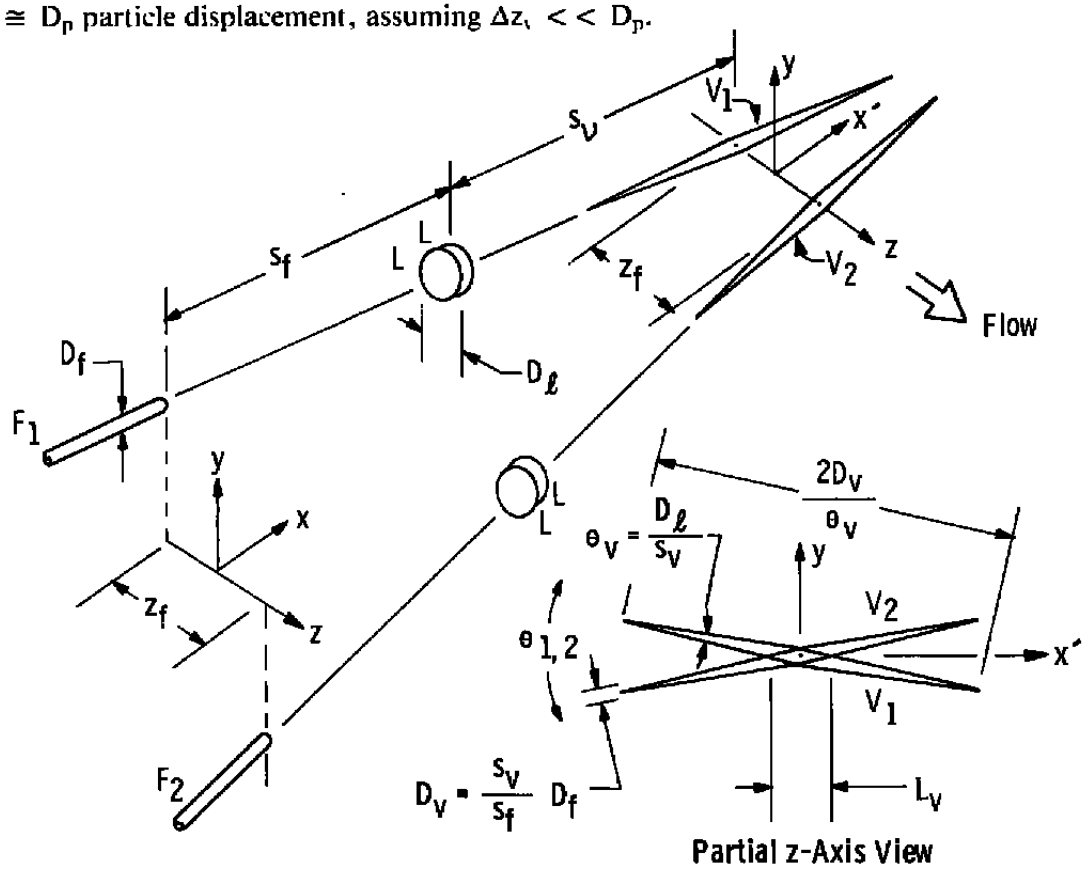

Figure 3. TEV geometry configured for small probe volume length and minimal systematic measurement error.

*For very remote particle trajectories with finite (nonzero) lens aperture slit width, the signal duration slowly increases so that $\Delta z \cong D_p + D_v$ is not satisfied; in fact, $\Delta z >> D_p + D_v$ is satisfied. However, signals from such very remote probe volume positions are relatively very weak and therefore are usually ignored by an electronic signal processor.

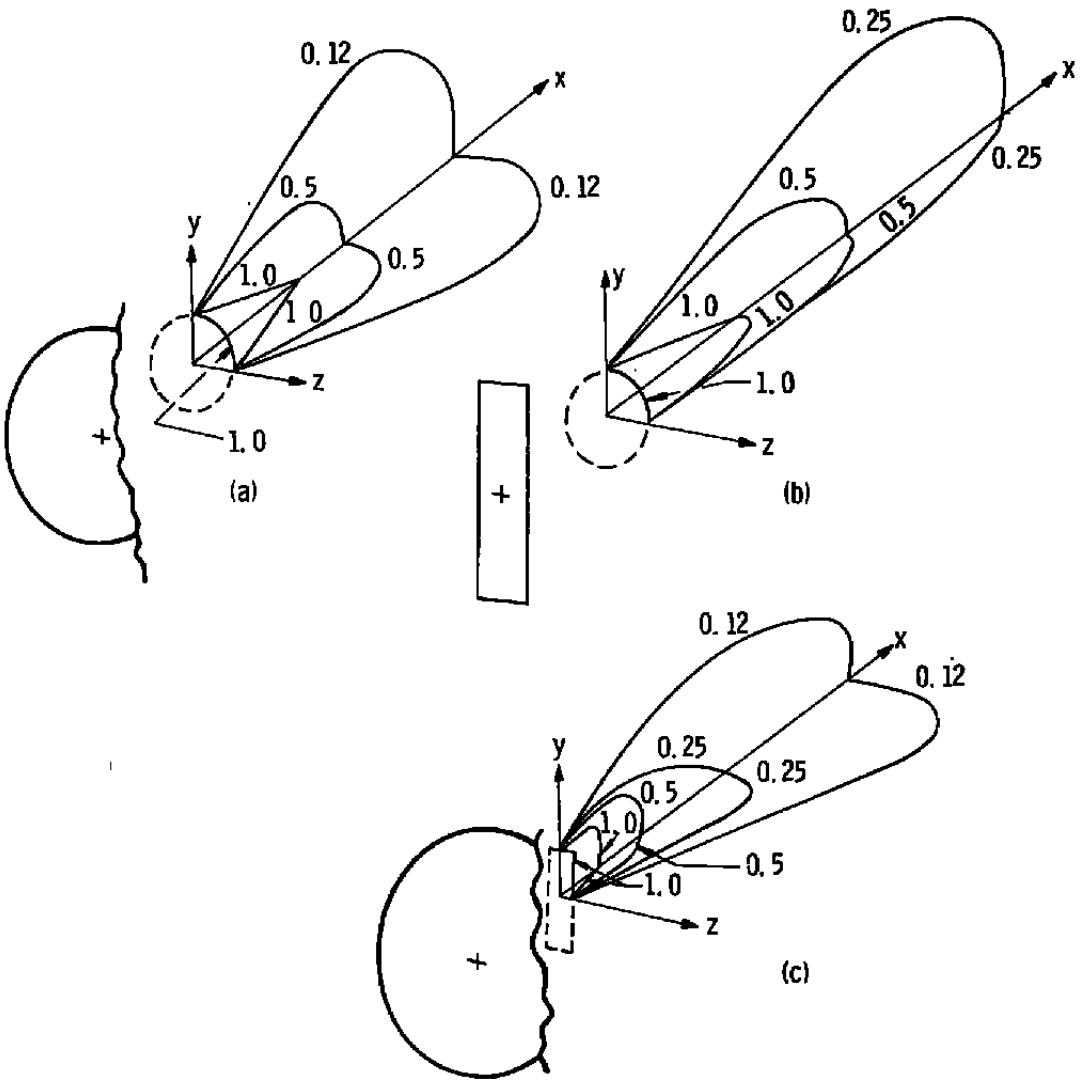

Figure 4. Approximate xz and xy plane radiation collection efficiency contour plots for three different geometries of collecting lens aperture and virtual aperture.

Case 1, which can be used to reduce the z-axis widths of the remote regions of the two TEV probe volumes, represents the TEV geometry that is most often employed at AEDC. However, in one employment where much lower than usual accelerating gas and particle temperature was expected, this slit aperture was not used, allowing the full circular collecting lens aperture to gather light and produce maximum signal amplitude. Signal broadened data from the remote probe volume regions were minimized by choosing only the particular data samples that resulted from relatively large trigger level settings on the electronic signal processor (see Section 3.6.2 of this report).

Case 2, which reduces the z-axis width of the central region of the probe volume, has not been used to date. However, such an employment can potentially be used in conjunction with a TEV to measure the z-axis dimension of a translating particle and may be used for this purpose sometime in the future at AEDC. It is not difficult to envision a TEV-based system that simultaneously measures the velocity and two orthogonal dimensions of a translating particle.

Cases 1 and 2 can be effectively used in conjunction, i.e., deployed in the same single probe volume optical system, to simultaneously achieve the benefits of both. However, both cases contribute to a reduction of the toal number of signal photons detected from a translating particle.

3.4 TEV EXTRANEOUS RADIATION SOURCES

Various extraneous (noise) sources of optical radiation can be collected and detected to degrade the TEV performance. Such sources and their relative effects will now be discussed. The results of this discussion will be used in the next section to develop the conditions which must be achieved for proper TEV detection.

Extraneous, noise-contributing radiations not received from the hot signal particles in the TEV probe volumes can be categorized as either (1) direct, line-of-sight radiation components from remote particles, from a radiating accelerating gas, and from a hot radiating backdrop surface (via rays through the detection volume virtual aperture in line with the collection aperture, see Appendix B), or (2) indirect radiation components (from particle field, accelerating gas, cell lights, or whatever) scattered off the backdrop and then through the same high detectivity region of the probe volume in line with the detector optics aperture. The direct component that results from particles located in the remote, low-detectivity regions of the probe volume can be substantial to the point of obscuring the signal. Substantial obscuration would result, for example, if the particle field were dense enough that the detector could not see through to the relatively low-emittance backdrop because of particle blockage. This condition would occur frequently without a particle being located in the high-detectivity region of the probe volume if $n_p \pi D_v^3 (6\theta_c)^{-1} < 1$ and $\exp(-x_{pf} n_p A_p) << 1$ where $\pi D_v^3 (6\theta_c)^{-1}$ is the assumed approximate volume of the high detection region of the probe volume and $(n_p A_p)^{-1}$ is the mean free path of a light ray propagating through the particle field.

The indirect components of detected radiation result from radiation being scattered off the (assumed) diffusely reflecting backdrop. These components cannot usually be eliminated by reducing the diffuse scattering coefficient of the backdrop to a negligible value as (1)

most low-scatter, high-absorbing optical surfaces, such as flat black paint or black optical felt, will diffusely scatter at least a few percent of the incident radiation, and (2) a high spectral reflectivity or mirror surface, which will scatter typically a few tenths of one percent, only reflects or deviates the line-of-sight of the detector package to another backdrop surface, and does not, by itself, provide a solution.

The relative detection of a particular extraneous radiation component is governed in part by the position in space from which it originated; the collection efficiency analysis of Appendix B can be used to determine the relative contribution versus spatial position of any component. For example, it can be shown that if the number of particles that illuminate the backdrop originates from a relatively small (in comparison to x_{vb}) bounded region, then the radiated particle field component that is diffusely reflected off the backdrop is negligible (relative to signal) if (Ref. 2)

$$x_{vb}^2 >> A_v \ (1 - \alpha_b) \ N_p/\pi \tag{3}$$

In this equation, x_{vb} is the distance between the probe volume and the backdrop surface, A_v is the probe volume virtual aperture area, $(1 - \alpha_b)$ is the (assumedly) diffuse reflection coefficient at the backdrop, and N_p is the total number of particles in the particle field (those radiating at the backdrop).

3.5 TEV DETECTION CONDITIONS

The results of the previous section and of Appendixes A (thermal emission characteristics), B (radiation collection efficiency) and C (signal-to-noise analysis) can be employed to quantitatively describe the conditions for which accurate TEV detections will be made. Such conditions for detection will be outlined in this section.

For a TEV system employing a high-responsivity PMT and a time interval counter type of signal processor to extract data effectively, the following conditions must be met: (1) the detected thermal radiation quantum number (photons) resulting from a single particle traversing the high-detectivity region of a probe volume, assuming no background radiations are present, must be great enough to produce large inherent signal-to-noise ratio (or SNR, see Appendix C); (2) the mean detected level of background radiation (photons/second), assuming no principal particle is present, must be significantly less than the detection level when a principal particle is present, and (3) the particle number density,

n_p (assumed uniform over a depth x_{pf}), must be low enough such that $n_p << V_v^{-1} + (\bar{A}_p\, x_{pf})^{-1}$, where V_v is the volume of detection* of a single TEV probe region, $\bar{A}_p$ is the mean particle cross-sectional area, and x_{pf} is the x-dimension or depth of the particle field. The detected photon quantum number of condition 1 above is dependent upon (1) the blackbody thermal emission characteristics of the particle surface (Appendix A), (2) the efficiency with which the thermal radiation is optically collected (as discussed previously and in Appendix B), and (3) the detector characteristics (as discussed previously for the PMT detector).

If these detection conditions are not met, it is doubtful that a time interval counter (signal processor) can be employed effectively; however, in some cases, other signal processing means more capable of extracting periodic data from noisy environments may possibly be used. For example, if condition 1 is not met but the inherent single particle SNR is low and of approximate value SNR $\cong$ 1, then a correlation-type signal processor would provide a good opportunity to extract data from the near side of a particle field, regardless of conditions 2 and 3. For condition 1 with SNR $<<$ 1, conditions 2 and 3 must be approximately met for even a correlator type to extract data in a reasonable time

3.6 TEV SIGNAL CONDITIONING AND DATA ACQUISITION

Two methods of processing and recording TEV signals will be discussed. The first is crude but inexpensive and involves taking motion pictures of signals recorded on a CRT oscilloscope. The final system used a gated counter with programmable trigger levels interfaced to a microprocessor controlled data acquisition system.

3.6.1 Moving Pictures of Oscilloscope Method

The initial means of processing and acquiring TEV data was to take moving pictures of the signal displayed on an oscilloscope. The optical signals from the two probe volumes were detected on a common PMT detector. A very sensitive movie film (ASA 400 color film, push-processed to ASA 800), a motion picture camera optimized for low light level, and an oscilloscope designed to record high-speed, single-swept events were used to record TEV data. The scope was operated in a single horizontal (time) sweep mode with the (normally manually controlled) horizontal sweep reset command signal being automatically delivered by, and synchronized to, the motion picture camera. To accomplish the latter, a circuit was developed to automatically rearm the oscilloscope horizontal sweep immediately upon each opening of the motion picture camera shutter. After each rearming, the first signal (if any)

*The detection volume or probe volume is the volume within which a particle must be to be detected.

meeting the qualifications of the oscilloscope trigger circuit would be displayed on the CRT and recorded on film. Using this method, individual TEV signal events were recorded at the frame rate of the motion picture camera, nominally 15 to 75 frames per second.

3.6.2 Computer-Controlled Counter Method

The final choice of a TEV signal processing and data acquisition system basically consisted of a 20-psec resolution, programmable electronic counter, an electronic timer, a flexible magnetic storage disk, and a graphics display terminal, all interfaced to a microcomputer. The counter was operated in the time interval measurement mode to process TEV signals, and its start-stop channel trigger levels were programmed by the microcomputer. The timer was started at the beginning of a data run to correlate acquired data with time.

Such a system provided the major benefits of (1) automatic progression during a run through a range of trigger levels sufficient to obtain TEV data under most tunnel conditions, (2) acquisition and storage of data at high rates, and (3) automatic reduction and plotting of data following the run. The computer was programmed to hold and acquire data at each trigger level for a time that was sufficient (e.g., 0.1 sec) to obtain a large data sample. The typical HEAT facility run time was only a few seconds. Without automatic, step-by-step ranging of the trigger levels during a run, a few unnecessary preliminary runs would be required to establish trigger levels for each new set of arc heater conditions.

A microcomputer with 28K 16-bit words of memory was used to control the counter trigger levels and to acquire, store, and display the counter and timer data (Fig. 5). TEV time interval counter data and timer data were stored on the magnetic flexible disk for permanent retention and were later reduced, displayed, and copied in a velocity histogram format.

Figure 6 is a flow chart of the computer program used to control trigger levels and acquire TEV data. A combination of FORTRAN and assembly language programming was used to implement this flow chart. Trigger levels are changed by factors of two (40 mV, 80 mV, 160 mV, etc.) every 100 msec during a run. Each time a new trigger level is selected, information on the memory location where data from the previous trigger level were stored is maintained so that data can later be analyzed by trigger level. After seven levels have been programmed (700 msec), the sequence of trigger levels repeats. This sequencing allows at least some data to be recorded throughout the run, regardless of signal level variations. Following an initial data run to establish the range of pulse heights, the number and range of trigger levels programmed may be reduced.

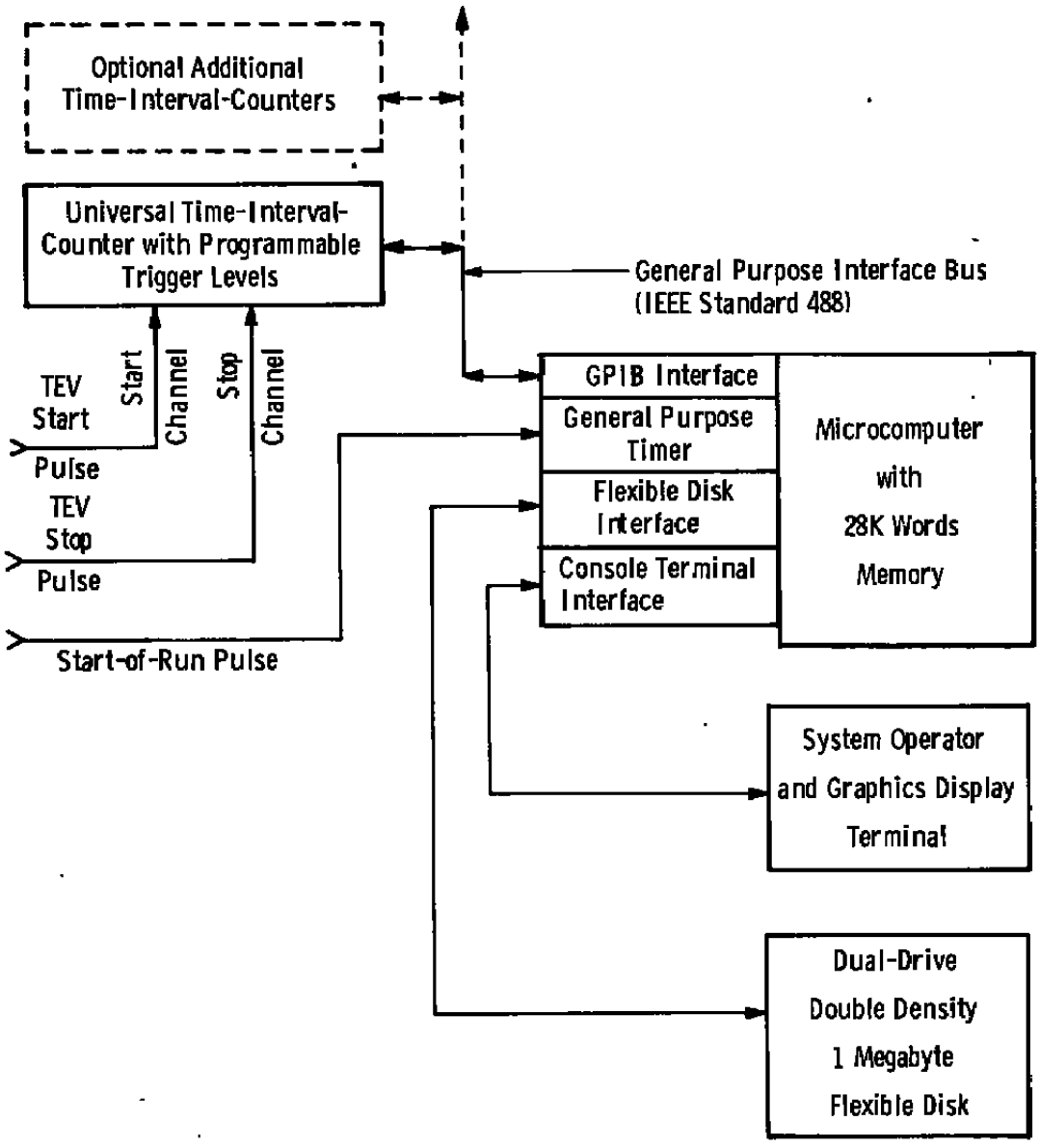

Figure 5. Data acquisition system.

Data from the TEV time interval counter was rounded to the nearest nanosecond and stored in computer memory as a 16-bit unsigned integer in the range 0 to 65,535 nsec. The value of run time from the general purpose timer was stored to a resolution of 10 msec as another 16-bit integer. However, to conserve memory, run time was only stored with every tenth TEV reading. The average time required to read and store a single TEV reading was 600 μsec, which permitted in excess of 100 readings to be obtained at each programmed trigger level, provided the rate of TEV pulses was adequate. Data were stored in computer memory until either the maximum run time programmed had elapsed or until 15,000 TEV

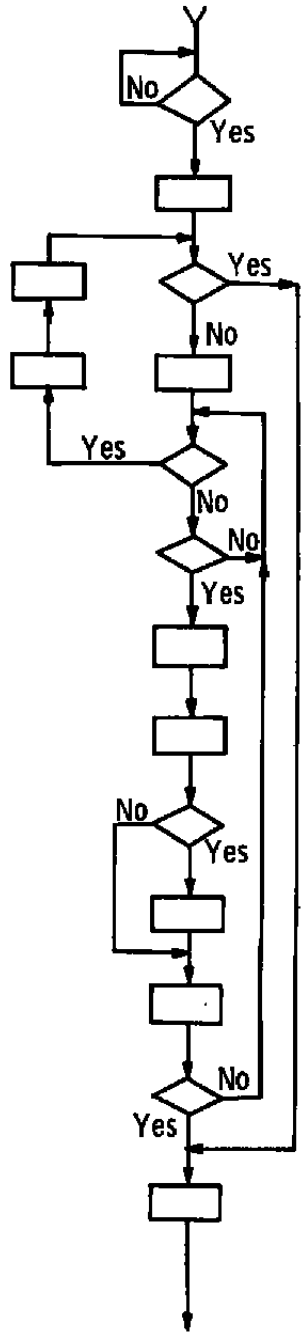

Begin

Has Start-of-Run Pulse Arrived?

N = 1, I = 1

Is N > 1,200?

Program the N^{th} Trigger Level*

Has N x 100 msec of Run Time Elapsed?

Is a Time Interval Counter Reading Available?

Input the Reading.

Store the Reading in Memory at Data Array Location I.

Is I a Multiple of 10?

Store the Current Run Time in Memory at Run Time Array Location I/10.

I = I + 1

Is I > 15,000

Store the Data Arrays from Memory on to Disk.

End

N = N + 1

Store I-1 (the Number of Readings Obtained Thus Far) in Memory at Correlation Array Location N.

*Trigger Levels Repeat in Cycles of 7.

Figure 6. TEV data acquisition program flow chart.

readings (memory capacity) had been acquired. The TEV data were then recorded on flexible disk and, if desired, read back and processed for display by trigger level.

3.7 TEV DATA

A typical TEV velocity histogram obtained from a HEAT facility is shown in Fig. 7. The velocity axis broadness of the data is attributable to a broad range of particle sizes being accelerated to different velocities by the expanding gasses in the HEAT nozzle. Individual particle velocities are detected to better than ±5 percent accuracy by the TEV. Such data compare well with data acquired using the streak photography technique.

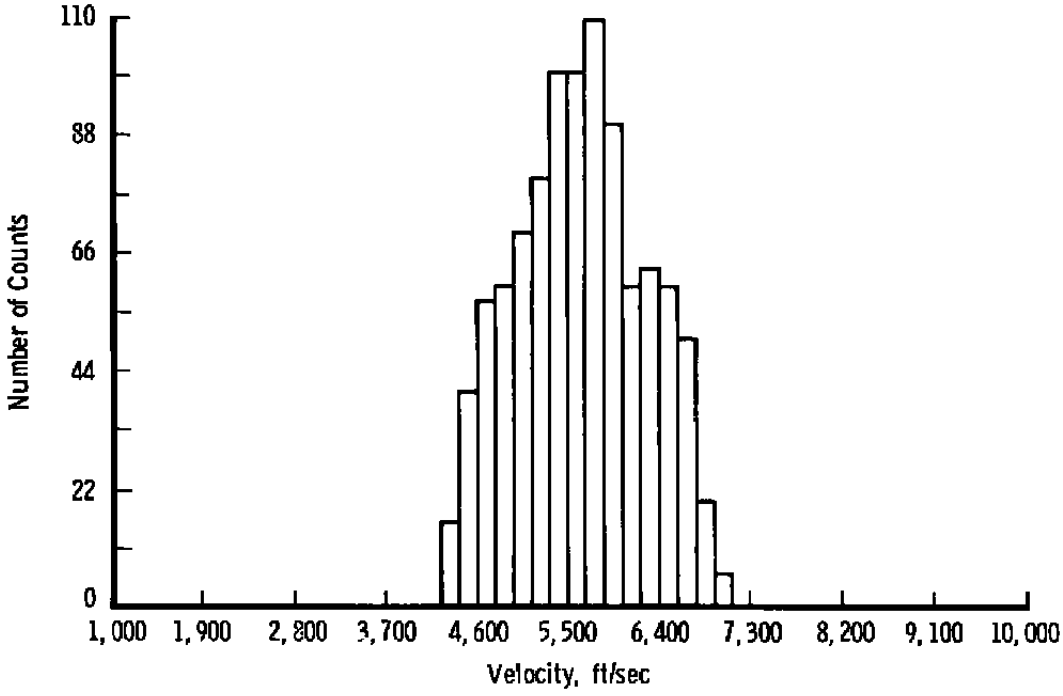

Figure 7. Typical TEV velocity histogram data.

4.0 DUST EROSION TUNNEL PARTICLE DIAGNOSTICS

The DET generates a high-velocity (1,000 to 3,000 $msec^{-1}$) dust cloud of large cross section (0.1- to 0.4-m diameter) and low number density (resulting from 100 gm sec^{-1} maximum particle mass injection). The mean particle size ranges from a few tenths of a millimeter to one millimeter average dimension (the particle shape is irregular, nonspherical). Optical access to the test section is provided by pairs of opposing windows viewing transversely through the dust cloud jet with one window on each side of the test section.

Over the years, various optical instrumentation techniques have been used to calibrate the DET particle fields. A pulsed laser holographic technique (Refs. 1 through 3) was employed to measure particle size, velocity, and number density; a laser velocimeter (Ref. 4) measured particle velocity; and an optical fiber-optic technique (Ref. 5) was used to measure particle size. Much of this data is summarized in a report describing the DET facility and its calibration (Ref. 6). More recently, an optical particle rate (number/time) monitor was employed to measure the instantaneous local particle rate throughout a run by photodetecting and counting the number of beam power reductions as particles intercepted a small laser beam. This instrument provided data for a nominal 3:1 particle size range, and it is believed that two of these instruments would provide data over the full 10:1 range of mean particle size that is characteristic of the DET facility operation. Futhermore, recent results indicate that by separately photodetecting the interruptions of many closely spaced, small laser beams by individual particles, size and velocity, as well as relative contribution to rate per unit area, can be measured. Such a laser multibeam system will be discussed in the later sections of this report. The particle rate monitor instrumentation will now be described.

5.0 PARTICLE RATE MONITOR

The particle rate monitor employs a laser beam of special geometry that is transmitted through the DET particle field. Individual particles of the low number density particle field intercept the beam and produce transient reductions of beam power. These are detected and counted using a PMT, a special pulse discriminator circuit, and an electronic counter operating in the event counting mode. Individual particle interruptions are counted over fixed intervals of time, and accumulated count data and time data are periodically recorded on the magnetic tape of a microprocessor-based data acquisition system.

5.1 PERFORMANCE CHARACTERISTICS

The general performance characteristics of the particle rate monitor system developed at AEDC will now be presented. The rate monitor output (counts per second) will be seen to vary in proportion to the local particle rate per unit area (or the local particle mass flux, mass/area/time). A signal-to-noise ratio discussion will be used to determine the minimum rate monitor optical beam power.

The optical geometry of the particle rate monitor beam is shown in Fig. 8. A truncated cone geometry laser beam (see Appendix D for particle rate monitor optics) converges to a minimum-diameter disk slightly smaller than the smallest particle size to be detected. The beam then diverges symmetrically about the minimum diameter. The point of minimum cone diameter is positioned in front of a model being tested. The detection cross section, or

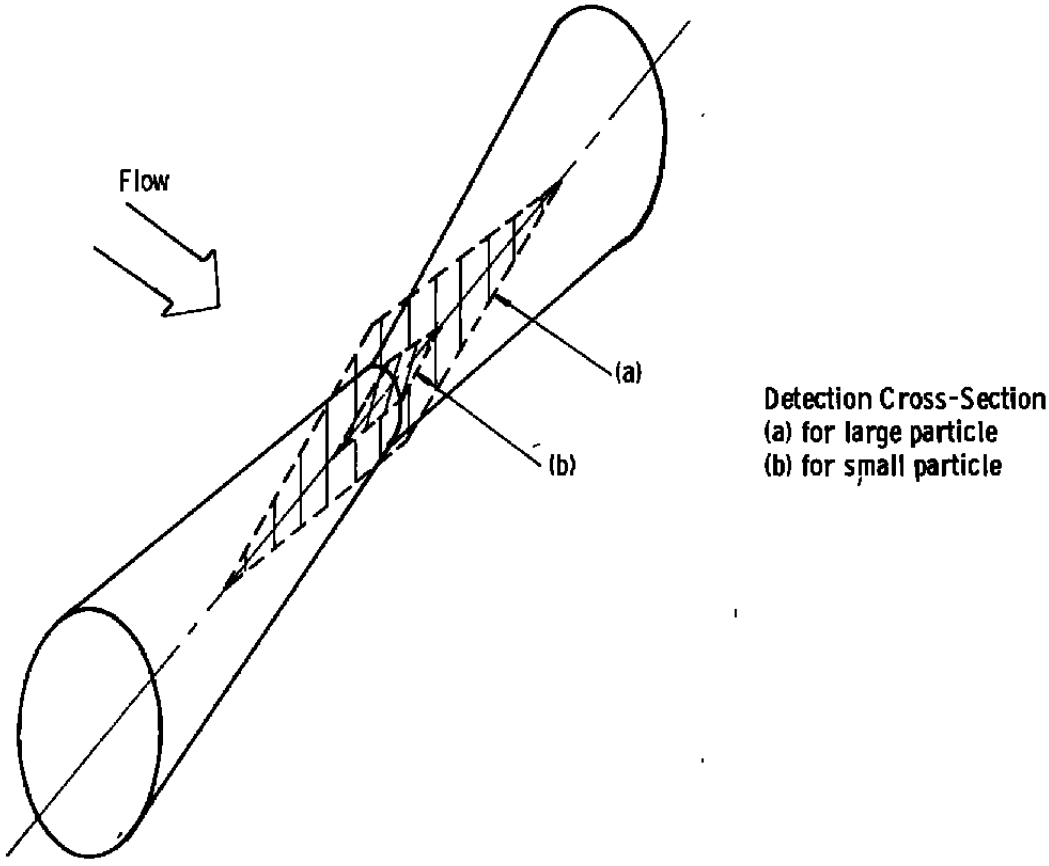

Figure 8. Particle rate monitor beam.

the area through which a particle center must pass to be detected, is based on a particle blocking a specific minimum fraction (50 percent or more, for example) of the laser beam; the detection cross section of both a small and a large spherical particle is indicated in the figure. For a particle to be detected, the center of the assumed spherical particle must intercept the detection cross section or detection area.

The rate monitor output count rate is proportional to a local count rate per unit area even though the system detection cross section varies with particle size. If the dust injection rate is doubled, for example, the rate monitor detection rate doubles for all particle size ranges and therefore its cumulative output rate doubles.

It is advantageous that the detection cross section increases as particle size increases. This is because particles of larger (mass weighted) mean size can be injected only at lower number per second rates and therefore require a larger detection cross section to accumulate a large data sample in a given time. Also, one beam geometry can be effectively employed for a

range of particle sizes. To date for the DET application, a 500-μm cone minimum diameter has been used to detect chiefly in the 400- to 1,000-μm range.

For design purposes it is necessary that the cone minimum diameter be an appreciable fraction of the mass-weighted, mean particle size so that the many small particles usually present in a sample having a large mean particle size will be discriminated out and not detected. Otherwise, it is possible that the accumulated count data would not be representative of the large particles that dominate the model erosion process.

The convergence-divergence angle of the cone beam is also important. First, it determines, in part, the detection cross section and must be large enough to obtain a large number of particle counts per sampling interval. The relative trigger level of beam power reduction also determines the detection cross section. Second, a large cone angle limits the longitudinal dimension of the detection cross section, permitting monitoring of particle rate in an area of flow more representative of an immersed test model than the entire flow area.

Finally, the cone beam effective geometry can be altered by changing the trigger level, as discussed in Appendix E. The truncated cone geometry of Fig. 8, for example, can be achieved only by employing a high (90 percent) relative trigger level setting.

5.2 INHERENT SIGNAL-TO-NOISE RATIO

Assuming that the detected level of background radiation is negligible relative to the RM beam power, then accurate count data are obtained if the RM beam power at detection, p, produces a high inherent signal-to-noise ratio (SNR $>>$ 1). The effective detection time interval is determined by the electronic bandwidth, Δf, of the threshold trigger circuit of the electronic counter. The intrinsic or inherent SNR is thus (see Appendix C)

$$\mathrm{SNR} = (\gamma p \beta / \Delta f)^{1/2} \qquad (4)$$

where γ is the beam power trigger level setting relative to the total cone beam power p, and β is the PMT cathode photoelectron yield (photoelectrons per joule). For example, an SNR of 20 is generated with a 50-percent trigger level ($\gamma = 0.5$) of a $p = 10^{-5}$ watt beam with $\Delta f = 10^8$ Hz and $\beta = 10^{16}$ per joule.

5.3 SIGNAL CONDITIONING AND DATA ACQUISITION

The signal conditioning and data acquisition systems used with the rate monitor system will now be discussed. Problems relating to a time-varying level of window contamination

and low optical beam power will be overcome, in part, by improving the signal processing electronics. The final data acquisition system will monitor two counters, one of which totals signal pulses and the other, clock pulses.

Initially, to acquire data with the particle rate monitor system, a zero-crossing detector (ZCD) was used to compare the instantaneous PMT signal voltage to a fixed reference voltage; the ZCD outputted a level change when the two voltages became equal. ZCD output level changes were electronically counted over fixed time intervals to produce rate monitor data. A commercially available, IEEE-488 bus-compatible electronic counter operating in an event-counting mode was employed. However, the initial system was not satisfactory because it produced inconsistent data.

The cause of this data inconsistency was attributable to two undesirable characteristics observable in the PMT detector output signal. First, the signal was noisy partly because of the moderate SNR of the detected optical signal (quantum noise) and party because of the included electrical noise induced by the nearby 5-MW arc heater generating the facility flow. Second, window contamination resulted in attenuation of the signal beam and a slow decrease of the mean signal level detected during a run. Both problems had to be compensated for to extract usable information.

The tunnel windows, which provided optical access to the test cell, slowly became contaminated during the run. The rate of this contamination was not necessarily constant, resulting in a detected beam power that continually decreased in an unpredictable manner, often to only 25 percent or so of the original prerun values. Since the events to be detected were also characterized by a partial beam blockage and a corresponding detection level change, some means to discriminate between the two events had to be developed. A characteristic of the events that differed significantly between the two was the relative time duration of each, the drop in signal caused by a particle blockage occurring over a much shorter time than the gradual attenuation of the signal attributable to window contamination. Therefore, a circuit was developed to supply to the ZCD a varying threshold or reference voltage equal in amplitude to a percentage (corresponding to beam blockage by a spherical particle of a given size or larger) of the time-averaged, low-pass-filtered signal level. This effectively caused the attenuation of the beam, caused by window contamination, to be invisible to the ZCD's.

The low SNR condition was dealt with by increasing the optical beam power and by adding variable hysteresis to the ZCD circuitry. The beam power was increased by adding lens L1 of Fig. D-1. The relative amount of hysteresis, again as a percentage of the variable low-pass-filtered PMT signal level, was selectable by setting two 10-turn potentiometers.

The final data acquisition system for the particle rate monitor consisted of a graphic microcomputer system and two electronic counters operated in an event-counting mode, interconnected by an IEEE-488 bus. One counter was connected to the signal-conditioning electronics and maintained a running total of valid events (particles blocking a predetermined percentage of the beam). The second counter had as its input a 10-MHz clock and functioned as a time reference. The microcomputer read the contents of both counters approximately four times per second and stored the information on magnetic tape.

5.4 DATA

Typical RM data are shown in Fig. 9. Note that the dust was turned on and off periodically during a run as different models were injected into the test region. The RM data showing large fluctuations in dust rate from model to model have correlated well with net model erosion measurements taken after a run.

This completes the discussion of the RM system. A related electro-optical system, also applied to DET, is the laser multiple-beam particle diagnostic system. This system will now be presented.

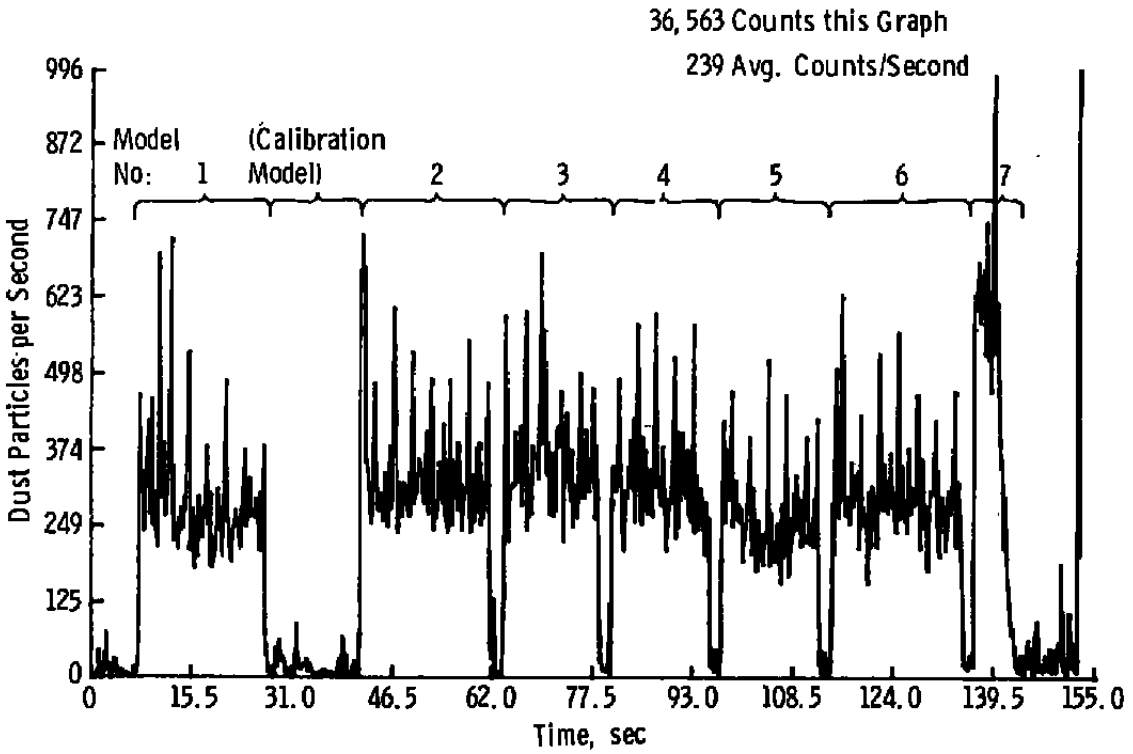

Figure 9. Typical rate monitor data.

6.0 PROTOTYPE LASER MULTIBEAM PARTICLE DIAGNOSTIC SYSTEM

Methods to measure particle velocity and mass flux, based, respectively, on detection of thermal emission from hot particles and detection of the interruptions of a single laser beam by optically opaque or irregularly shaped particles have been previously presented and discussed. The theory and application of a multiple laser beam particle diagnostic system, or simply multibeam system will now be presented. Such a system detects the presence of an individual particle in its detection region and measures its size and velocity. From an accumulation of data records, the system semiquantitatively measures the variation with particle size of (or the relative contribution of a particle's incremental size range to) the particle rate per unit area. This laser multibeam system is basically similar to, and is an extension of, the particle RM system discussed previously and, like the RM system, has been applied to the DET at AEDC. However, unlike the rate monitor, the multibeam system is in an early stage of development.

6.1 OPTICAL CONFIGURATION

The general laser multibeam particle diagnostic system uses four laser beams that propagate through the particle field and terminate onto three PMT detectors, with two of the beams intercepting a common detector. The geometries of the four beams in the probed region are specifically configured by the illuminating optics into two pencil-like beams, one cone-like beam (consisting of two truncated cones, end-to-end, connected by a short length of right circular cylinder) and one ribbon-like beam (Fig. 10). The centerlines of all four beams are parallel. The cone and ribbon beams are separately photodetected on two PMT's, and the two optically identical pencil beams are optically combined and simultaneously detected on a third photodetector.

The intensity distribution (w/m^2) of the four laser beams will be assumed as an approximation to the actual intensity distribution, (1) to be both y-axis and z-axis invariant within the confines of the beam and zero outside, (2) to be uniform (constant) in x for small values of x (such that $|x| < F/2$) within the collimated or depth-of-field region of each beam, as illustrated, and (3) to vary as x^{-1} or x^{-2} outside this collimated region where $|x| > F/2$, for the ribbon beam and cone beam, respectively. Laser beams of this geometry and intensity distribution can be generated using an optical system similar to that discussed in Section 6.3 and in Appendix F. It can be stated without proof that if these approximate intensity distributions are used for data calculation purposes, the error introduced to beam measurements from which particle size and velocity are computed will be small, and only moderate error will be introduced into the computed particle detection cross-section values.

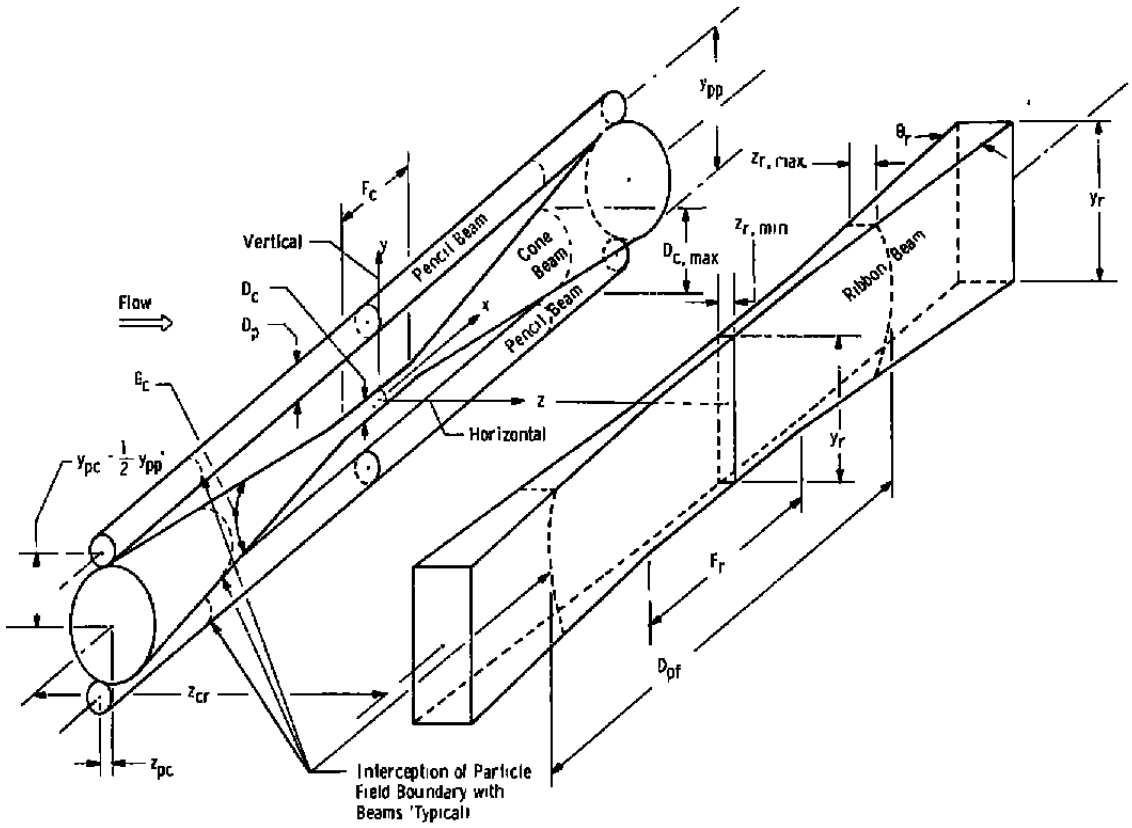

Figure 10. Optical geometry of the multibeams.

6.2 OPERATING PRINCIPLES

Consider a small particle moving approximately along the z-axis in the positive direction of Fig. 10. Let the particle be either opaque or of highly irregular geometry so that the power (w) of a beam intercepted by the particle will be essentially blocked (or scattered, or whatever) from contributing significantly to the uniformly diverging, unimpeded remains, if any, of the beam. Such a particle would initiate a voltage pulse in an auxiliary electronic circuit just at the instant when it blocked 70 percent of the cone beam, and would do so provided it did not simultaneously intercept more than 30 percent of the power of the combined pencil beams. For example, such an auxiliary circuit voltage pulse would be generated by particles 1, 2, or 3 of Fig. 11 but not by particles 4, 5, or 6 of the same figure. Spherical particles are shown in Fig. 11 for illustrative purposes only and such particles may not be properly detected by a multibeam system unless they were optically opaque. The auxiliary circuit pulse would be generated by opaque spherical particles, for example, within

a specific size range and only by those about to pass through approximately the central portion of the downstream ribbon beam. This pulse would then trigger the cathode ray tube (CRT) of an oscilloscope to sweep horizontally in time. The CRT vertical signal would be proportional to the sum of the auxiliary circuit output voltage pulse and the photodetected power of the ribbon beam (a longer duration voltage pulse occurring at a later time when the particle passes through the ribbon beam, see Fig. 12). The two signal voltages are added by employing an oscilloscope with two signal input channels and by operating it in the add mode. A typical CRT data record is shown in Fig. 12. Each CRT data record thus acquired would be photographed on motion picture film for permanent record. The film records the time between the upstream and downstream pulse events, from which particle velocity can be calculated. From the height and duration of the recorded downstream pulse event can be calculated particle vertical (y-axis) dimension and the maximum and minimum values of the ratio of particle horizontal (z-axis) dimension divided by particle velocity. The horizontal (z-axis) dimension of the ribbon beam is generally unknown because x-position is unknown but can be specified to be within minimum and maximum values; this permits the latter ratio (of horizontal dimension divided by velocity) only to be specified to lie within a range of minimum and maximum values.

Allowing measurement into the diverging part of the ribbon beam is not an ideal situation. However, only a prototype system is being discussed. A more ideal system would employ a more divergent cone beam or a wider (z-dimension) ribbon beam with a greater depth of field, or a combination of both.

Consider now what information can be obtained from a particle vertical size histogram which plots the number of detections versus particle vertical size. Such a histogram can be obtained from a large number of CRT records, and an example of such a plot is shown in Fig. 13.

The small particle data ($z_p < 2D_c$) on such a plot must be disregarded became of the cutoff in the ability of the cone beam to generate a trigger condition on small particles (see Fig. 14 which plots multibeam system detection cross section versus particle size and assumes spherical particles). The remaining large particle size (or dimension) distribution data semiquantitatively indicate the contribution of each particle size range to the rate per unit area. A more accurate conversion of the size histogram of the multibeam data to a more relevant size histogram of the number of particles per unit area existing in the particle field is beyond the scope of this report but could be obtained, assuming spherical particles, with the aid of Fig. 14.

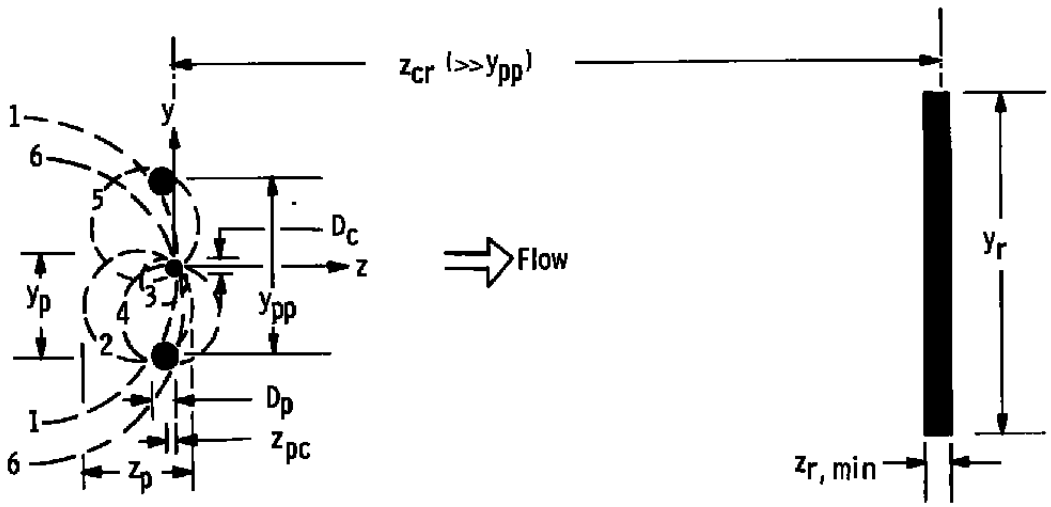

Figure 11. Cross section of multiple laser beams (shaded) at x = 0 showing 6 particles.

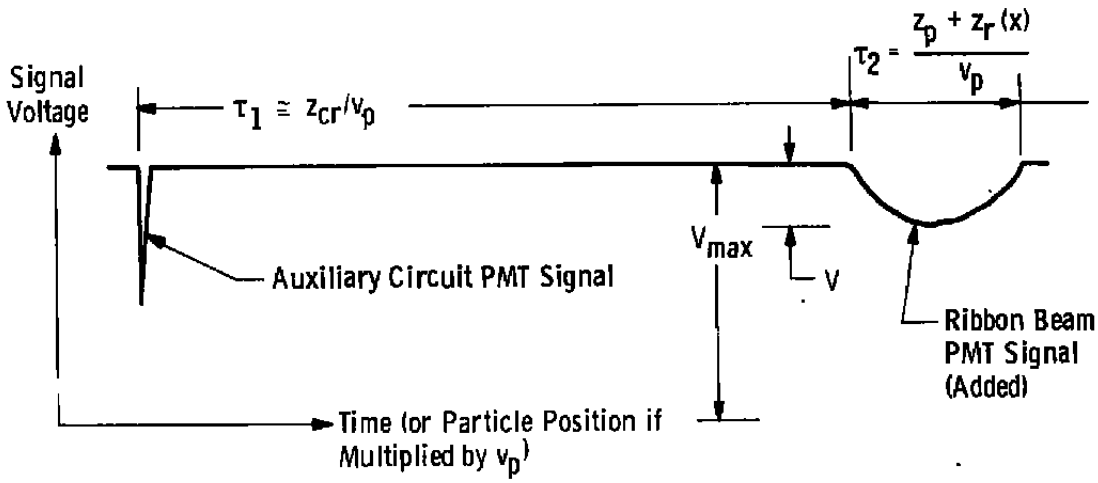

Figure 12. CRT record attributable to particle 2 of Fig. 11.

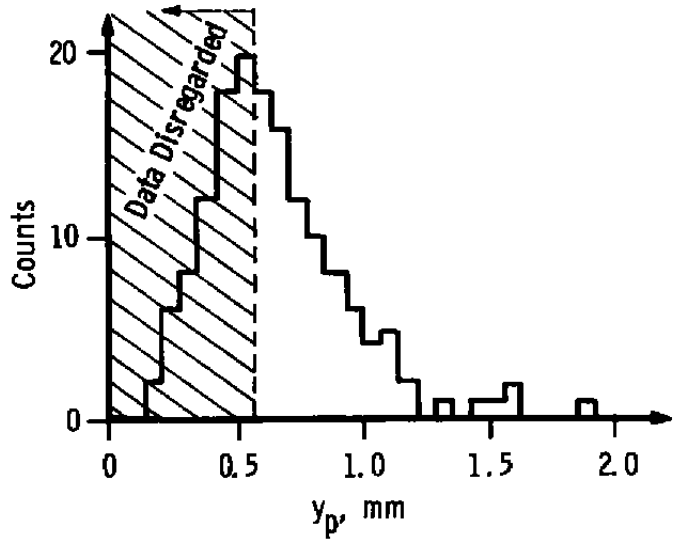

Figure 13. Typical particle vertical size distribution data.

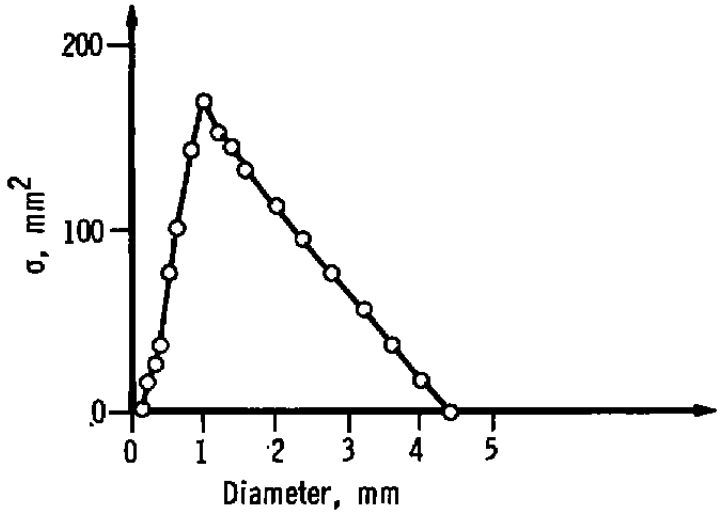

Figure 14. Multibeam system detection cross section versus particle diameter.

With the aid of Figs. 10 through 12, the particle horizontal or z velocity component, v_p, its vertical or y dimension, y_p, and its horizontal or z dimension, z_p, are given by

$$v_p = z_{cal}/\tau_1 \tag{5}$$

$$y_p = y_1 V/V_{max} \tag{6}$$

$$\frac{z_r + z_p}{v_p} = \tau_2$$

$$z_{r,\min} \leq z_r \leq z_{r,\max} \tag{7}$$

where all newly appearing quantities are defined in Figs. 10 through 12 and in the Nomenclature. By horizontal dimension or horizontal component of velocity it is intended to mean the projected size or projected component of velocity, as projected along the flow direction or z-axis and attributable to the particle being in the same orientation as when it passed through the detection region (and so on, for the vertical or y-axis dimensions and components). Equation (7) equivalently states that

$$\left.\begin{aligned} z_{p,\min} &= \tau_2 v_p - z_{r,\max} \\ z_{p,\max} &= \tau_2 v_p - z_{r,\min} \end{aligned}\right\} \tag{8}$$

where all quantities to the right of the equality sign are experimentally measured (Figs. 10 through 12). Thus, the minimum and maximum values of a particle's z-dimension are measured and not the z-dimension itself. This is because the time width of the particle derived ribbon beam signal is dependent upon the local width (z-dimension) of the ribbon beam and such dimension is generally unknown (or known only to within limits) if the particle passed through the diverging, noncollimated region of the ribbon beam (such that $\frac{1}{2}F_r < |x| < \frac{1}{2}D_{pf}$, see Fig. 10). Thus, because a time-of-flight measurement through the ribbon beam can be taken from either the diverging part of the ribbon beam as well as the collimated part, and, because it is generally not known from which part the measurement was derived, the horizontal dimension of the particle can not be known exactly; only the minimum and maximum values of this dimension can be determined. (This uncertainty of measurement can be eliminated by causing the diverging part of the ribbon beam to fall outside of the detection region; however, such a design change was beyond the proof-of-principle scope of the present study.

6.3 DESIGN FOR DET APPLICATION

A prototype laser multibeam particle diagnostic system was performance tested in the DET at the AEDC. The characteristics of the DET facility and its particle fields will first be outlined, and the specific optical design of the prototype system used will then be presented.

DET is an arc-heated, particle-injected flow-field facility used for model erosion testing and was briefly described in Section 3.0. Particle field characteristics typical of the DET are as follows: injected particle size varies from 0.200 to 1.000 mm; particle shapes are

nonspherical and generally highly irregular with a maximum to minimum dimension ratio of typically 2:1 to 5:1; the particle optical absorption coefficient is moderate (10 to 50 percent) for 0.650 mm or smaller mean size and high (50 to 100 percent) for larger sizes; particle velocity ranges from 1,000 to 2,000 $msec^{-1}$ for larger and smaller sizes, respectively; particle field diameter is nominally 230 mm; particle number density is 30 per cm^3 for smaller sizes and 3 per cm^3 for larger sizes.

The multibeam particle diagnostic system tested in DET was mounted on optical rails exterior to the DET test cell as illustrated in Fig. 15. To accommodate the multibeam system, the more easily aligned RM system was moved from the horizontal optical centerline position to the two opposing test cell windows and mounted at a 45-deg angle (Fig. 15).

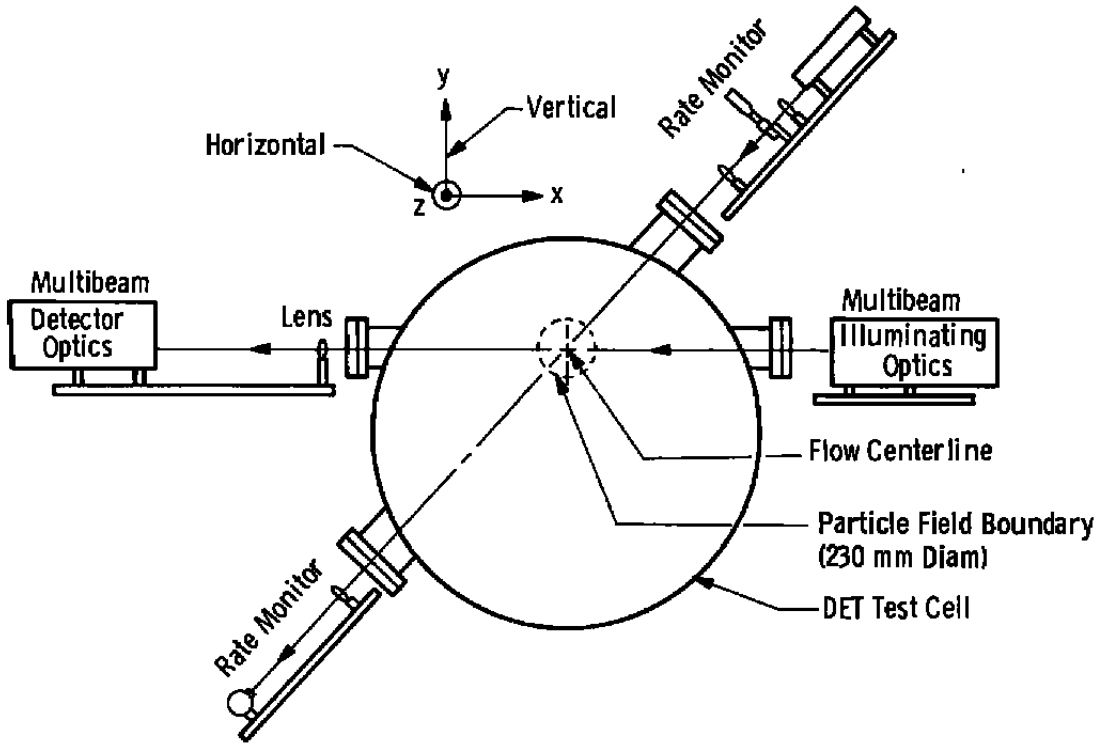

Figure 15. Dust erosion tunnel test cell instrumented by both rate monitor and multibeam particle diagnostic systems.

6.3.1 Transmitter Package

The multibeam system consisted of two separate electro-optical packages connected optically by a relay lens as illustrated in Fig. 15. The illuminating optics package (Fig. 16) contained the laser, a spatial filter and beam reducer subsystem, a one-dimensional or

anamorphic beam-expanding prism pair, a beam-splitting cube, an aperture mask (see Fig. 17) and pair of lenses that produced, by projection, a collimated, real image of the illuminated aperture mask at a 1-m working distance from the front of the package. Fig. 18 shows the light pattern at various longitudinal positions on each side of the collimated centerline image region. Note that the four beam centerlines remain collimated, the pencil-beams remain essentially the same size throughout the particle field, and the cone-beam and ribbon beam minimum dimensions increase by approximately a factor of two at the particle field edge (at $z = \pm 115$ mm). Further details relating to the transmitter package optical performance are given in Appendix F.

The mask geometries employed to detect the 0.65 mm and the 2.0-mm mean particle sizes in DET are shown in Fig. 17. As mentioned before, these were imaged 1:1 (with unity magnification) into the test region. Note that the only difference between the two masks is in the maximum dimension of the ribbon-beam aperture. The nomenclature 650/1,622, for example, of Fig. 17 is the ratio in micrometers of the mean particle size to the maximum cross-sectional (y-axis) dimension of the ribbon beam.

6.3.2 Receiver/Detector Package

The receiving and detection electro-optics package was linked to the illuminating optics by a relay lens. The relay lens, of focal length (F.L.) to serve the dimensions of the specific application, was placed two F.L.'s away from the detection region (the beam image region) and two F.L.'s away from the PMT detectors in the receiving package. This caused an image of the multibeam pattern of unit magnification to exist at the PMT's. The four-beam image pattern was projected onto three separate aperture masks, all similar to the aperture mask of the illuminating optics, but with oversized holes; each aperture mask was followed by a PMT detector. A series of beamsplitters and mirrors was used to divide the radiation onto three separate masked detectors. Certain holes in the three masks were taped closed, thereby allowing one mask to transmit only the two pencil images, one to transmit only the cone, and one only the ribbon. In this manner three separate PMT's in the receiving package detected individually the three components: (1) the sum of the pencil beams, (2) the cone beam, and (3) the ribbon beam.

6.4 SIGNAL PROCESSING

The cone-and pencil-beam PMT signal voltages were connected separately to an auxiliary electronic circuit which compared the instantaneous (broadband low-pass filtered) PMT voltage levels to the mean (narrow-band low-pass filtered) levels. A circuit output pulse (i.e., a level change of fixed, short duration) was generated when the relative instantaneous level

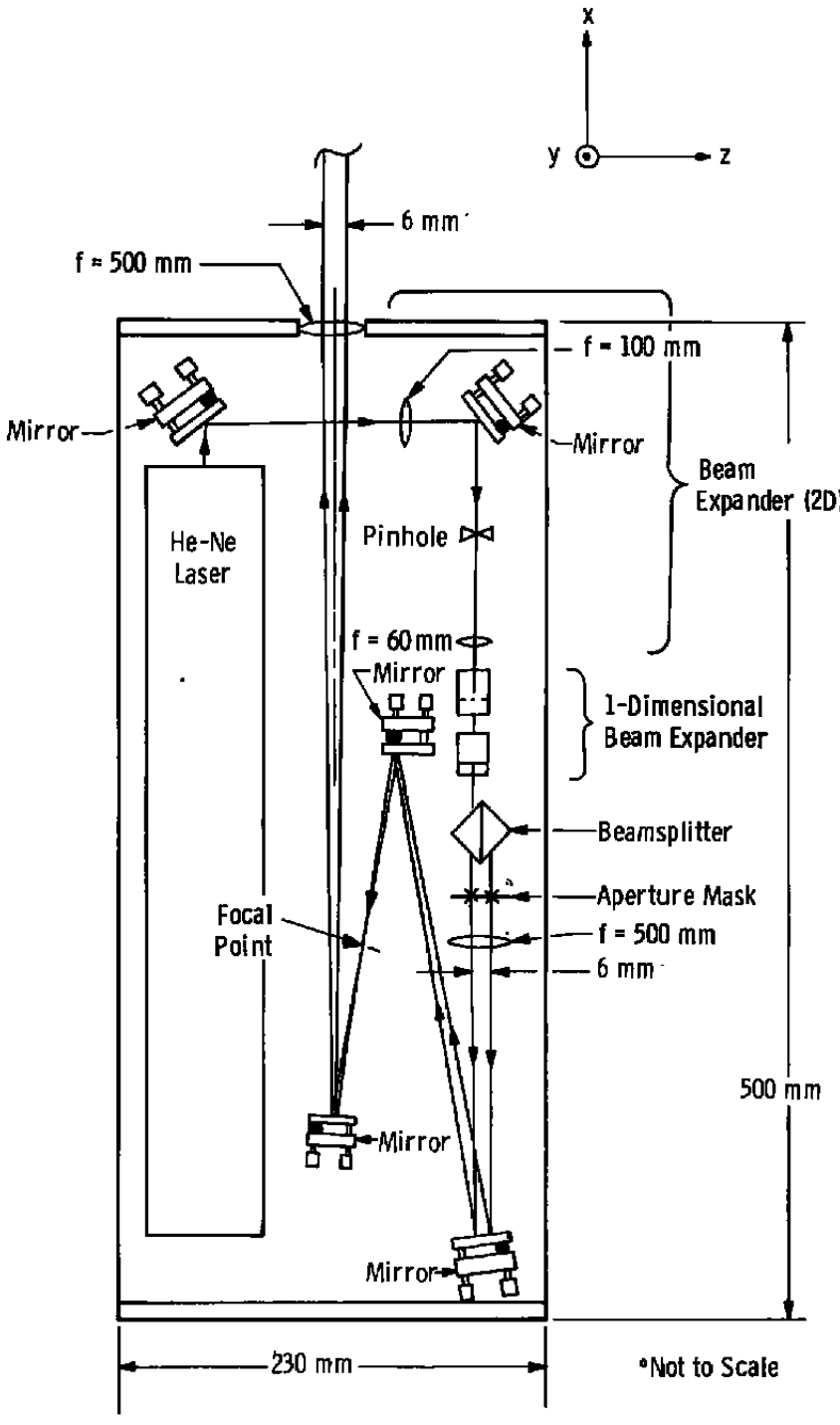

Figure 16. Multibeam illuminating optics.

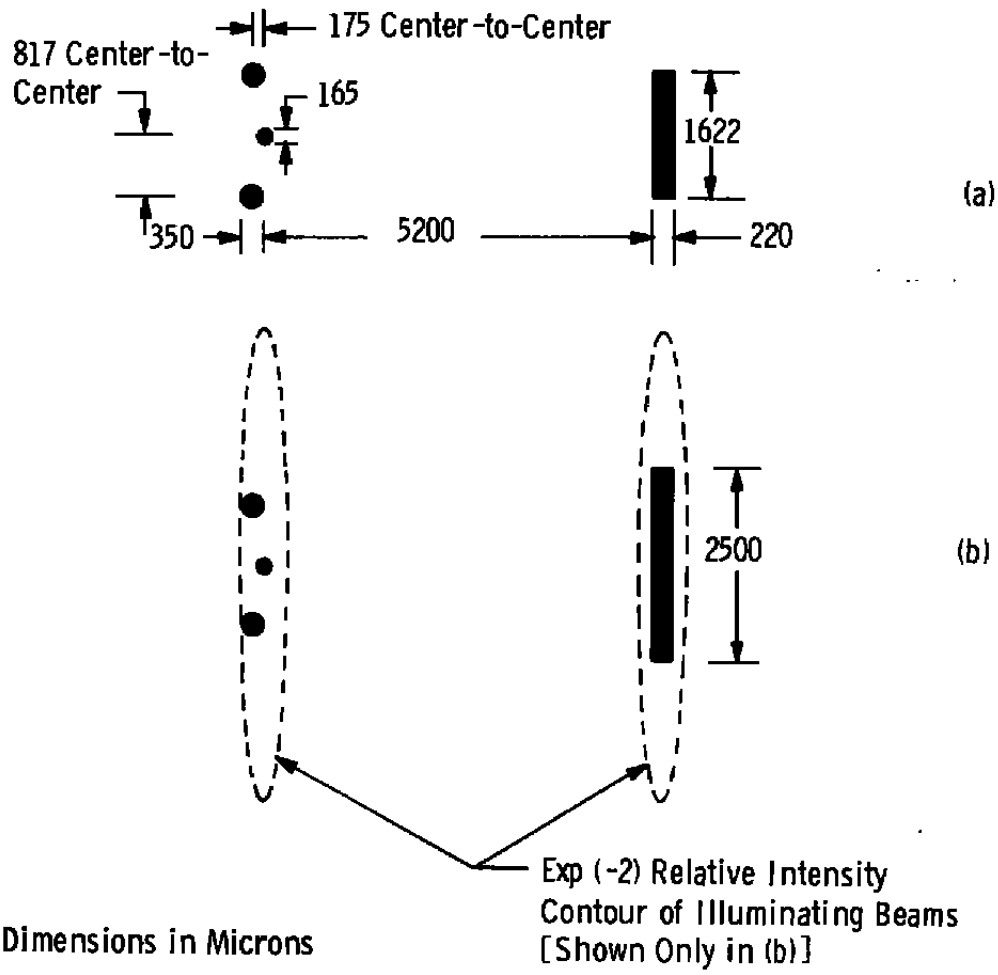

Figure 17. Transmission areas of the aperture masks for the experimental runs of (a) 650/1,622 and (b) 2,000/2,500.

of the cone beam increased through a set value and, simultaneously, if and only if the relative instantaneous amplitude level of the pencil-beam signal was below a second set value. The relative instantaneous level of the cone beam is the broadband low-pass filtered level divided by the narrow-band low-pass filtered level. The voltage comparator circuits included a variable hysteresis level setting to discriminate against noise. The output pulse triggered the CRT oscilloscope sweep, which displayed the summation of the output pulse and the ribbon-beam PMT signals. As described previously, this comprised a data record from which could be determined information relating to particle size, velocity, and relative contribution to rate per unit area.

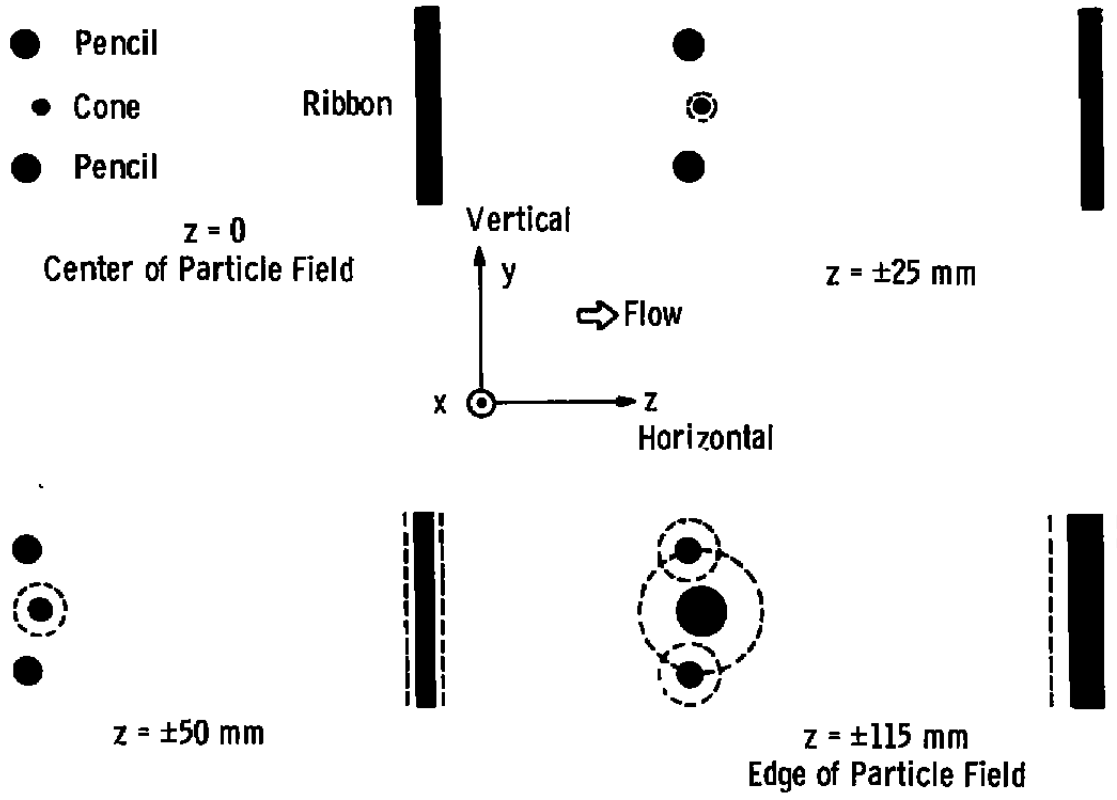

Figure 18. Light pattern of the multiple beams near focus showing (shaded) areas of 20 percent or greater individual beam intensity and (dashed) weak, first-order diffracted light.

6.5 EXPERIMENTAL RESULTS

6.5.1 Performance Testing

The multibeam system's optical performance was checked in the laboratory both by examining optically the collimated image probing (or detection) region and by introducing particle samples into this region. A 10- power (10X) magnifier was equipped with a 0.2 mm per division, metal-on-glass reticle onto which a 0.04-mm-thick, frosted, diffusely-scattering, semitransparent plastic tape was stuck. This scatter tape was illuminated with the multibeams, highly attenuated and near their image position. This scattered real image was viewed (10X) through the adjacent reticle. Such viewing was used to check that the aperture mask image magnification was indeed 1:1 and also to provide projected image size data for Fig. 18 which was used as a calibration. Also, typical DET particles were placed on a flat glass window and introduced into the multibeams with this viewing arrangement. It was observed a few millimeters downbeam of the particles that the particle shadows were largely dark and corresponded to the particle shape, as expected.

The auxiliary electronics circuit which generated the pulse to trigger the CRT time sweep was performance-tested in the DET tunnel. Two DET tunnel runs were used specifically for this purpose. On the first run the auxiliary circuit output pulse triggered the CRT sweep, and this pulse, added to the pencil-beam PMT signal, was recorded. There was no evidence that the pencil-beam signal was above its preset (trigger) amplitude on any of more than 1,000 records. On the second run a similar test was performed but with the cone-beam PMT signal substituted for the pencil-beam PMT signal. Again there was no evidence that the cone-beam power was below its minimum set level at the instant of trigger on any of more than 1,000 records. These tests established that the auxiliary circuit trigger pulse generating electronics performed correctly and reliably.

6.5.2 DET Data

Multibeam CRT data records for the two runs of 0.65-mm and 2.0-mm mean particle size were recorded on motion picture film. Data values for τ_1, τ_2, and V/V_{max} (Fig. 12) were measured manually and loaded onto magnetic tape. The data was then plotted, using automatic plotting software subroutines. Some of the data pertinent to this report appears in Figs. 19 through 34,with the 0.65-mm mean particle size data (650/1,622, Figs. 19 through 26) appearing in a group before the 2.0-mm mean size data. Horizontal and vertical dimensions (sizes) are the z and y particle dimensions parallel to the flow direction and the maximum transverse ribbon-beam dimension, respectively (see Fig. 18 and preceding discussion in Section 6.2). IE3 means that values are to be multiplied by 10 to the third power, or 1,000, etc.; 2,000/2,500 is the ratio of the injected mean particle size, in micrometers, to the ribbon-beam height dimension, in micrometers. Note that the ribbon beam height was varied, by taping, from a maximum value of 2,500 μm, to accommodate the two different mean particle sizes. MBPD means multibeam particle diagnostics. Much of the small particle size data is to be disregarded, as noted on many of the data plots. This is attributable to a reduction in the system's detection cross section for decreasing particle size, as discussed in Section 6.2 (see Fig. 14).

Specific error values for each data plot will not be discussed in much detail, as such information is beyond the scope of the present report. However, estimates of maximum error or error limits for the prototype multibeam system were as follows: particle velocity error, ± 5 percent; particle horizontal size error, ± 15 percent for sizes 0.5 mm and larger; particle vertical size error, ± 20 percent for sizes 0.5 mm to 2.0 mm; particle count error of size histogram plots, $+50$ percent to -10 percent for 0.6 mm and larger particle sizes; particle count error of velocity histogram plots, $+50$ percent to -10 percent for velocities corresponding 0.6 mm and larger particle sizes. These maximum error estimates are not indicative, in most cases, of the ultimate error achievable with a nonprototype system.

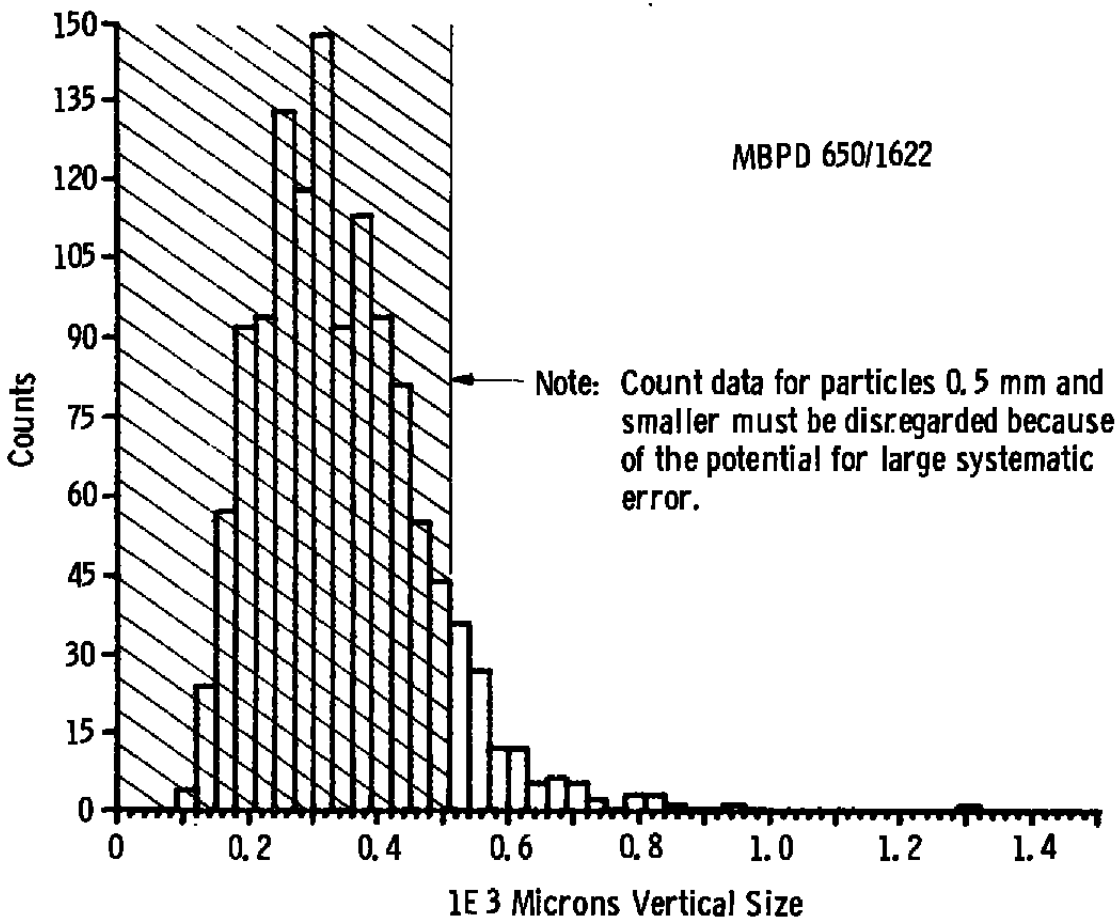

Figure 19. Vertical size distribution.

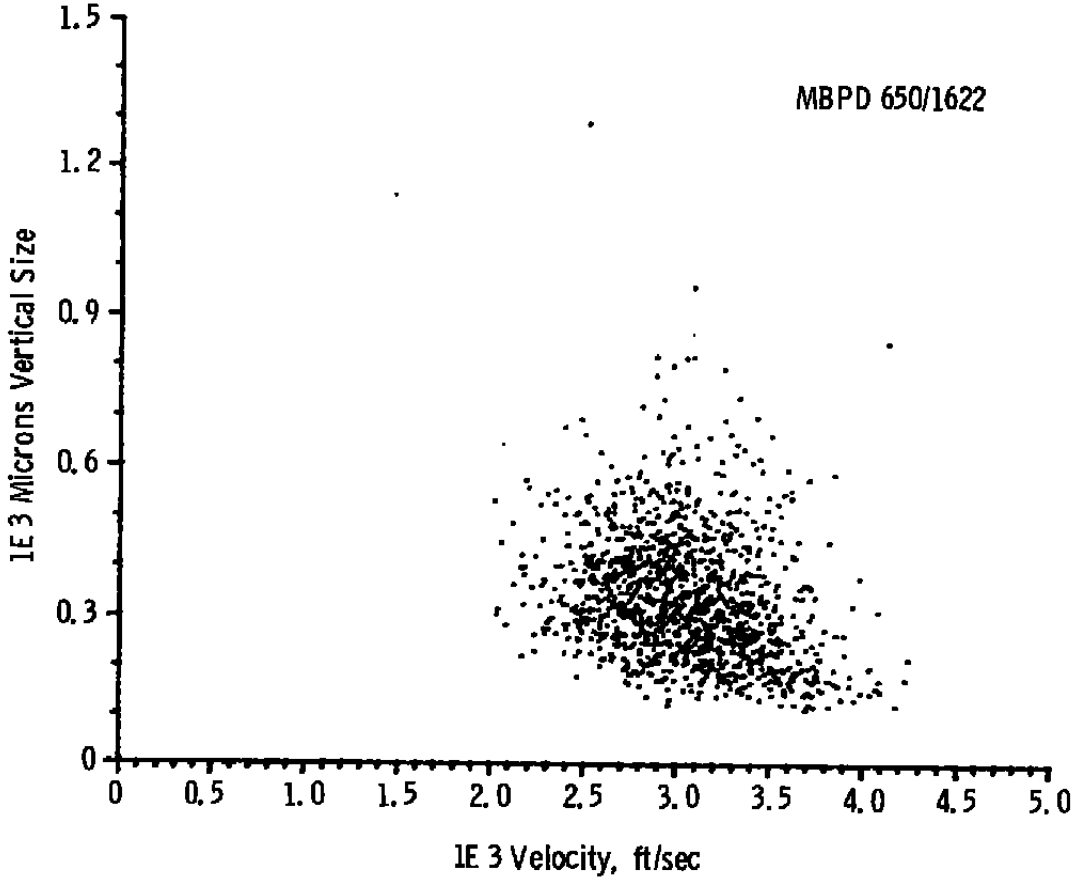

Figure 20. Vertical size versus horizontal velocity.

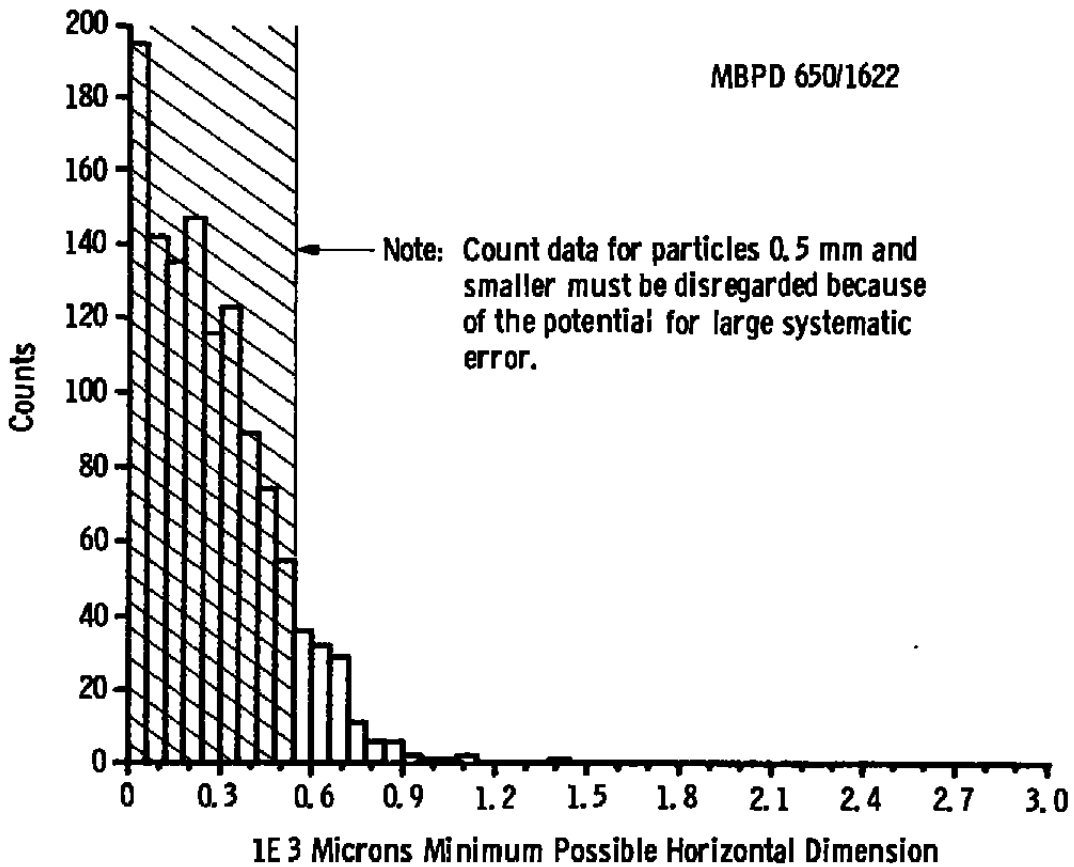

Figure 21. Distribution of minimum possible horizontal sizes.

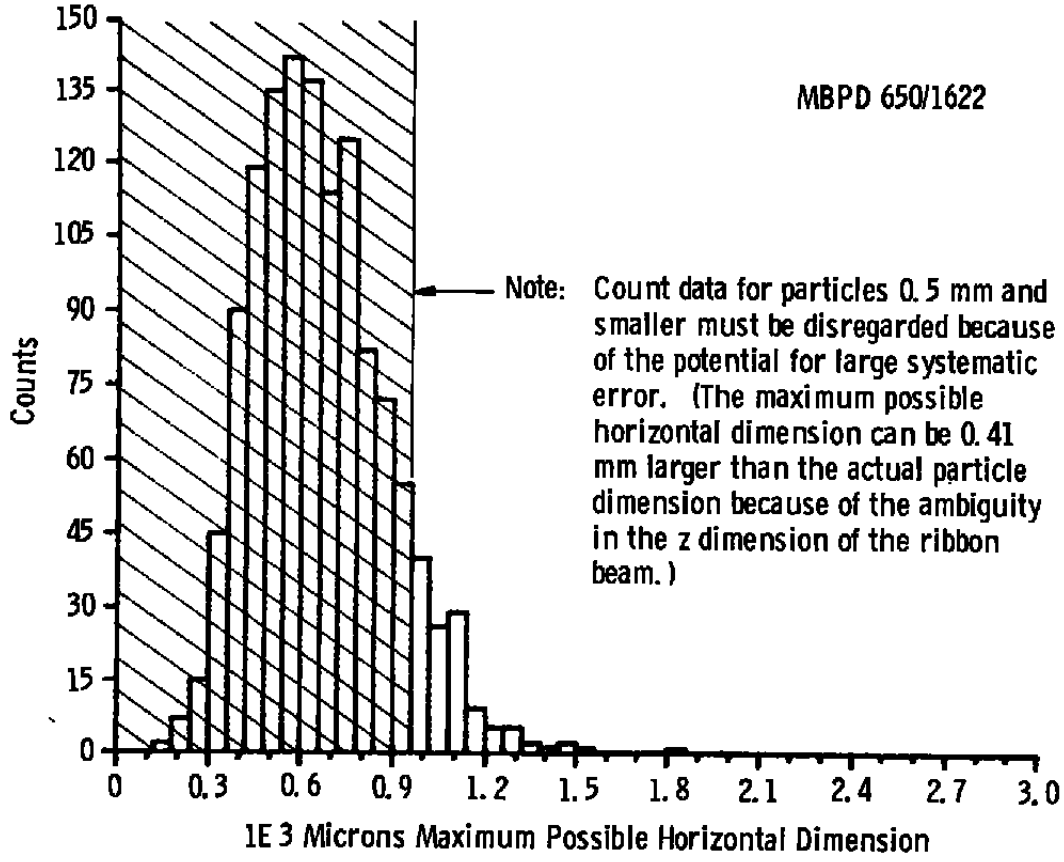

Figure 22. Distribution of maximum possible horizontal sizes.

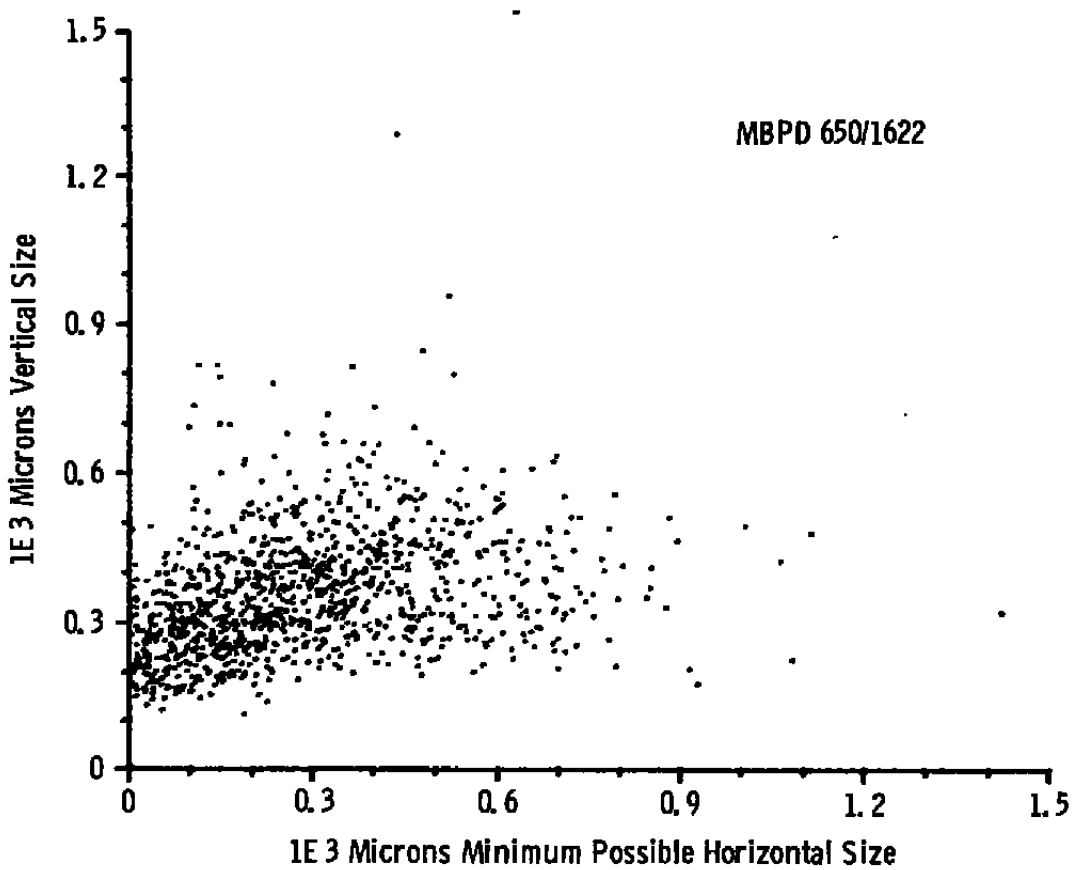

Figure 23. Vertical size versus minimum possible horizontal size.

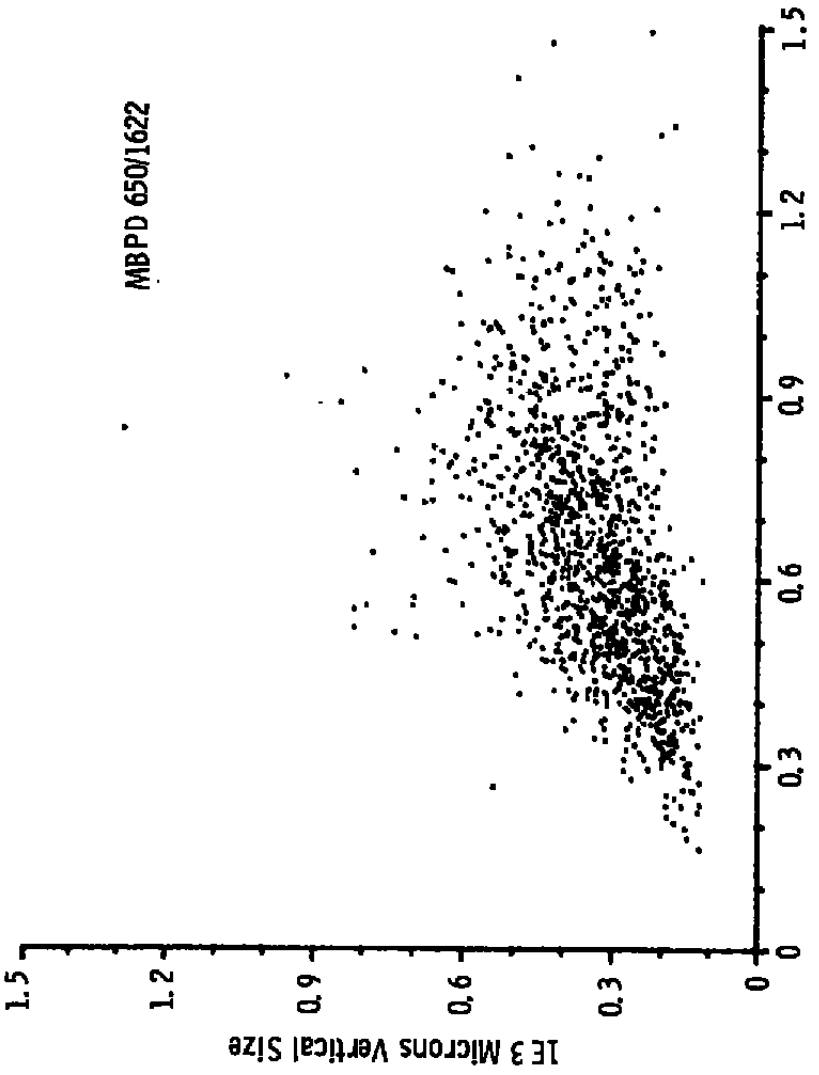

Figure 24. Vertical size versus maximum possible horizontal size.

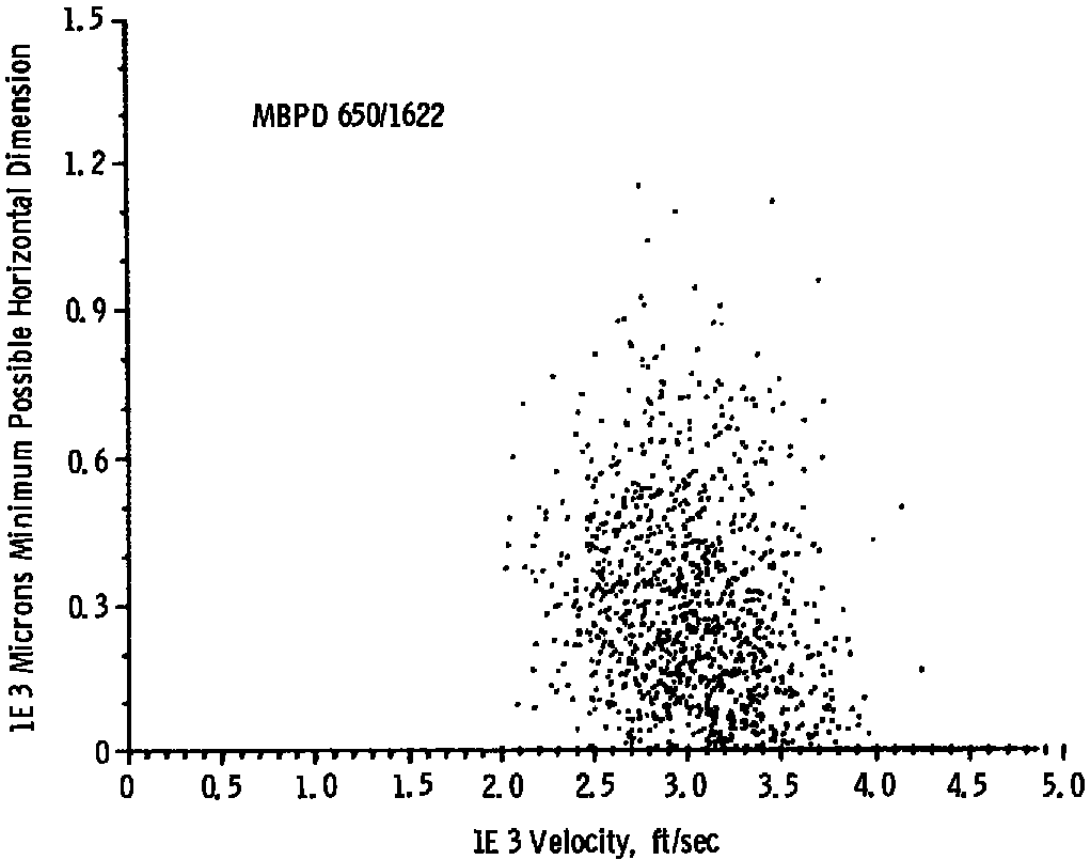

Figure 25. Minimum possible horizontal size versus horizontal velocity.

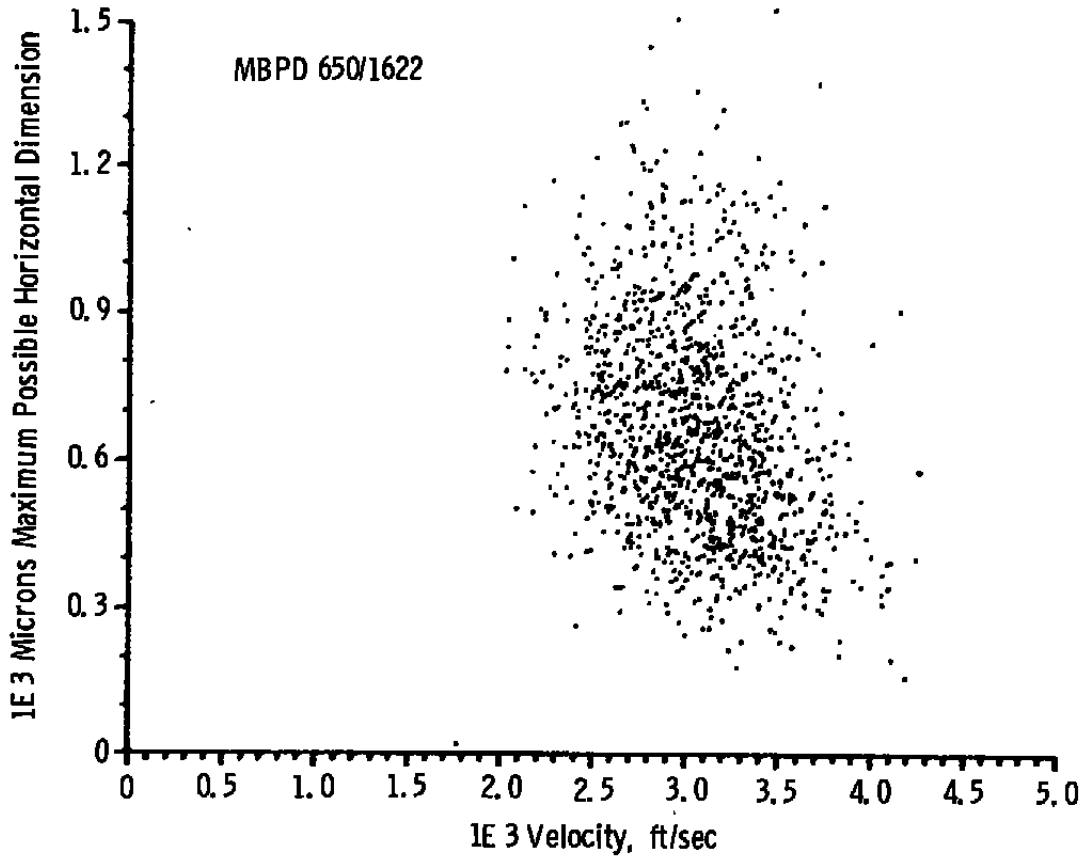

Figure 26. Maximum possible horizontal size versus horizontal velocity.

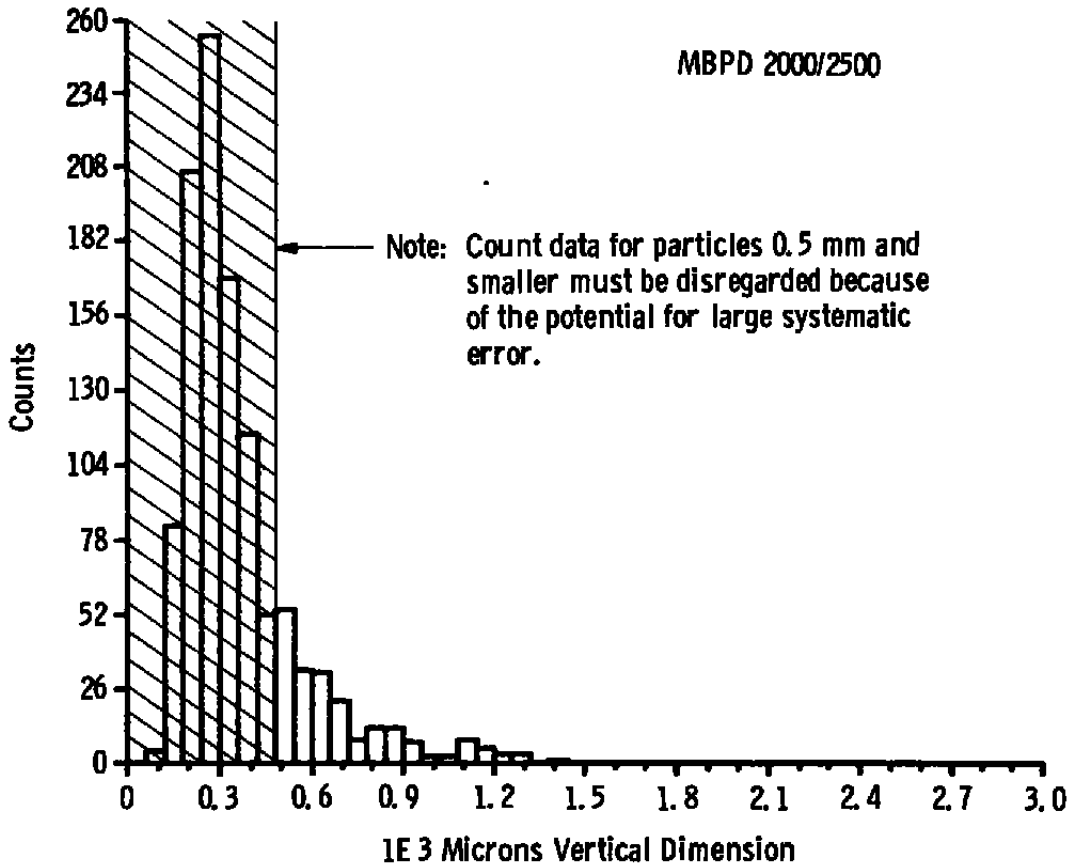

Figure 27. Vertical size distribution.

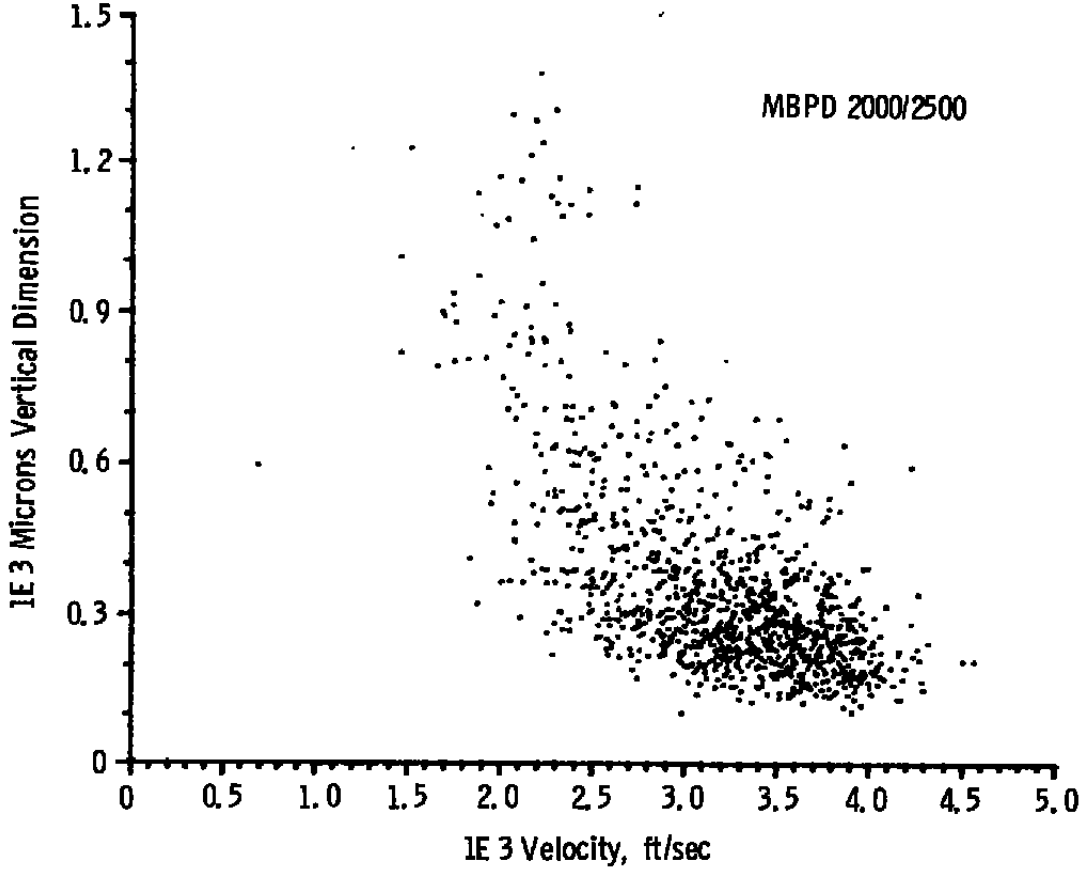

Figure 28. Vertical size versus horizontal velocity.

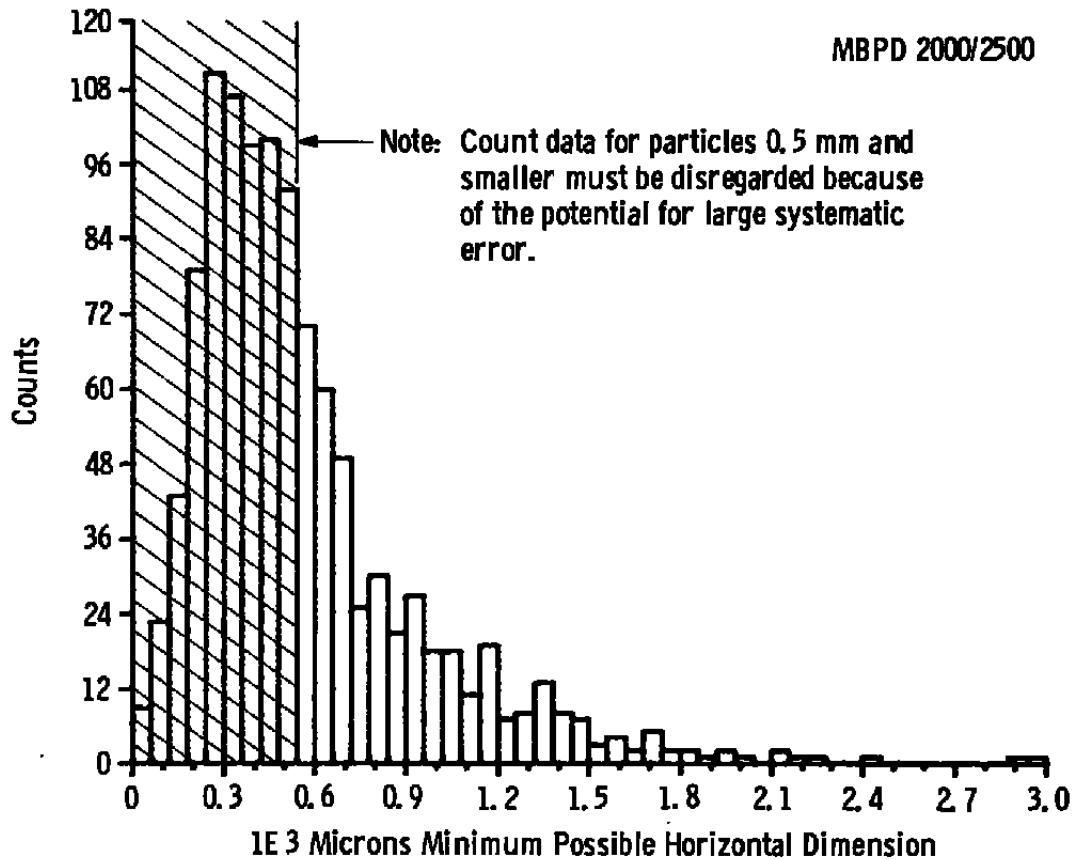

Figure 29. Distribution of minimum possible horizontal sizes.

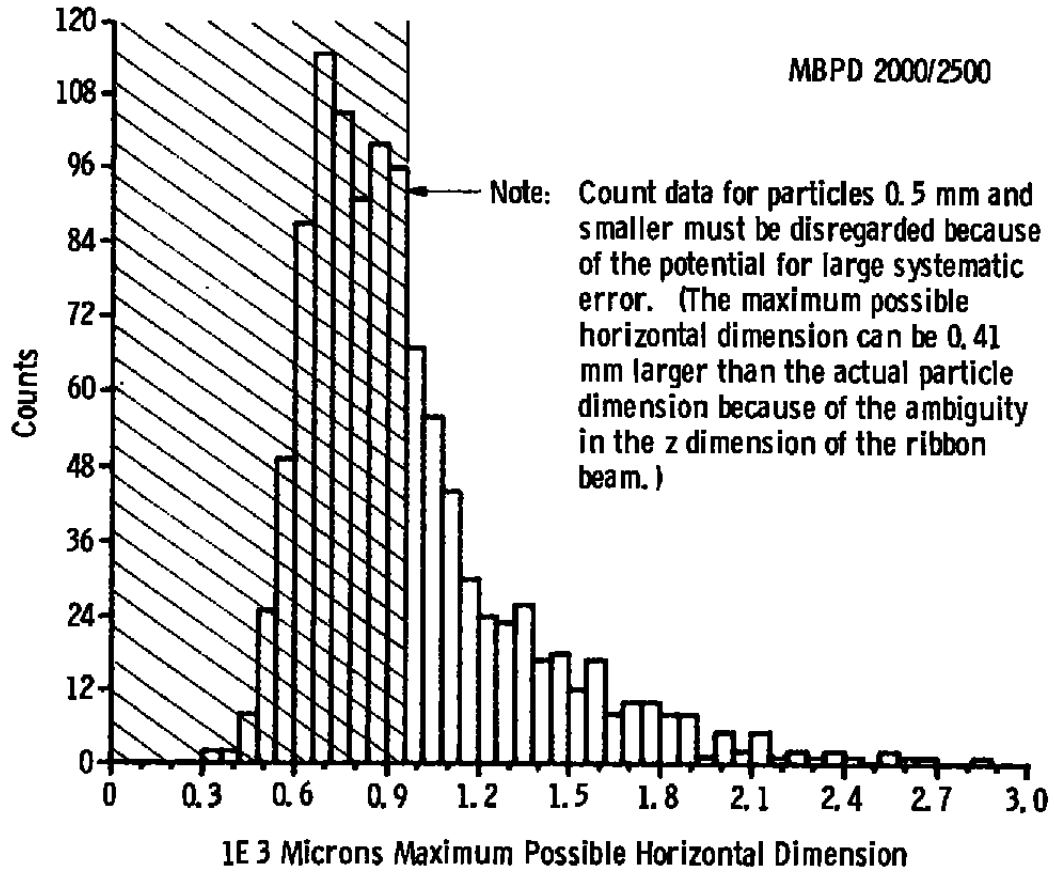

Figure 30. Distribution of maximum possible horizontal sizes.

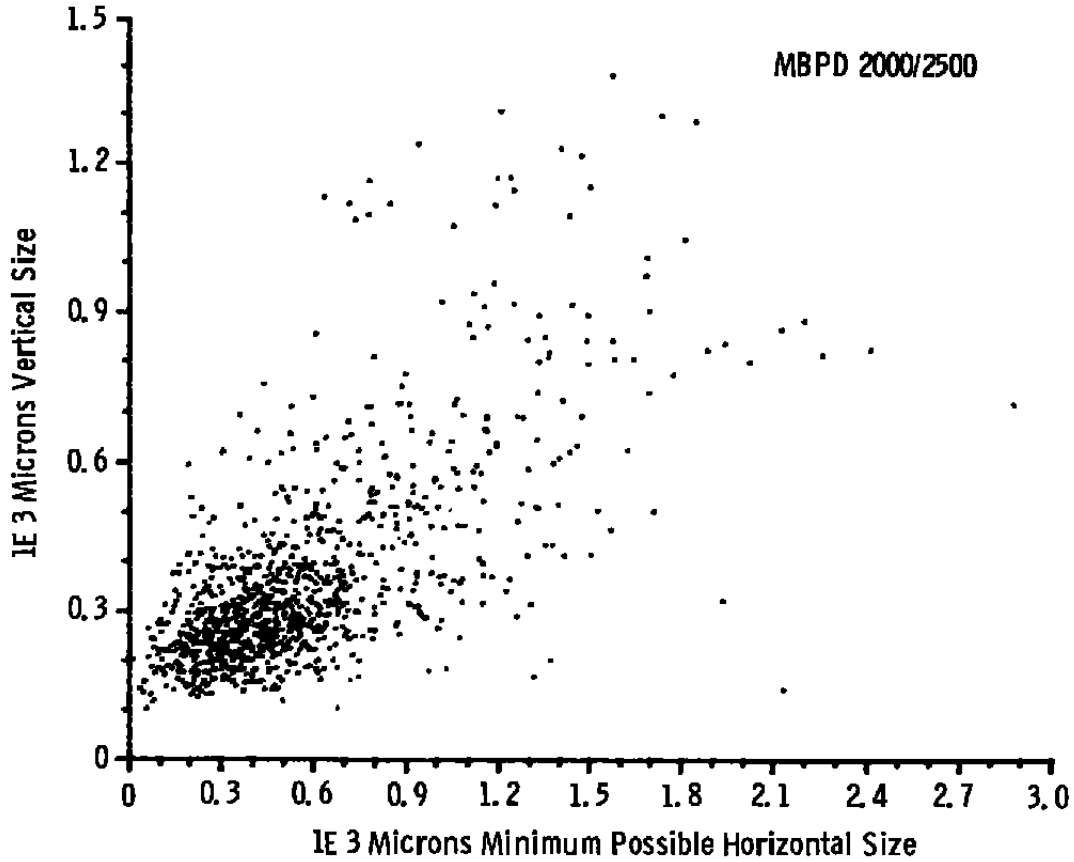

Figure 31. Vertical size versus minimum possible horizontal size.

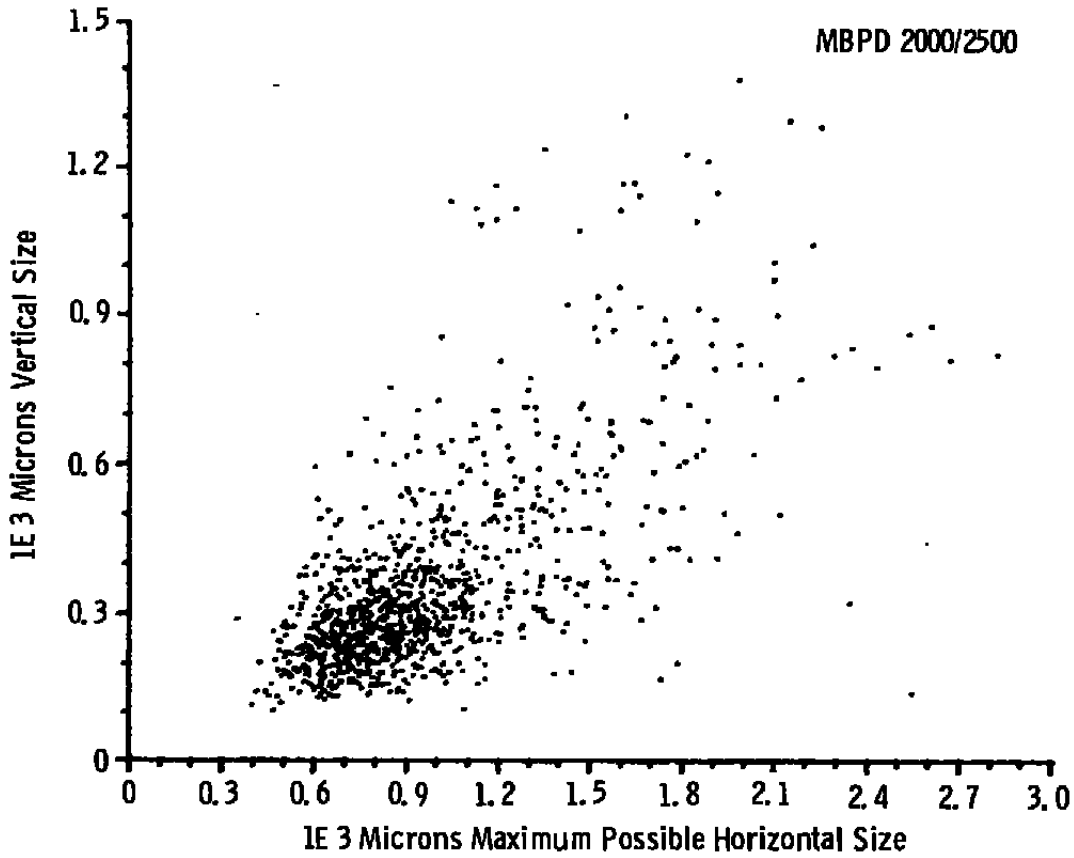

Figure 32. Vertical size versus maximum possible horizontal size.

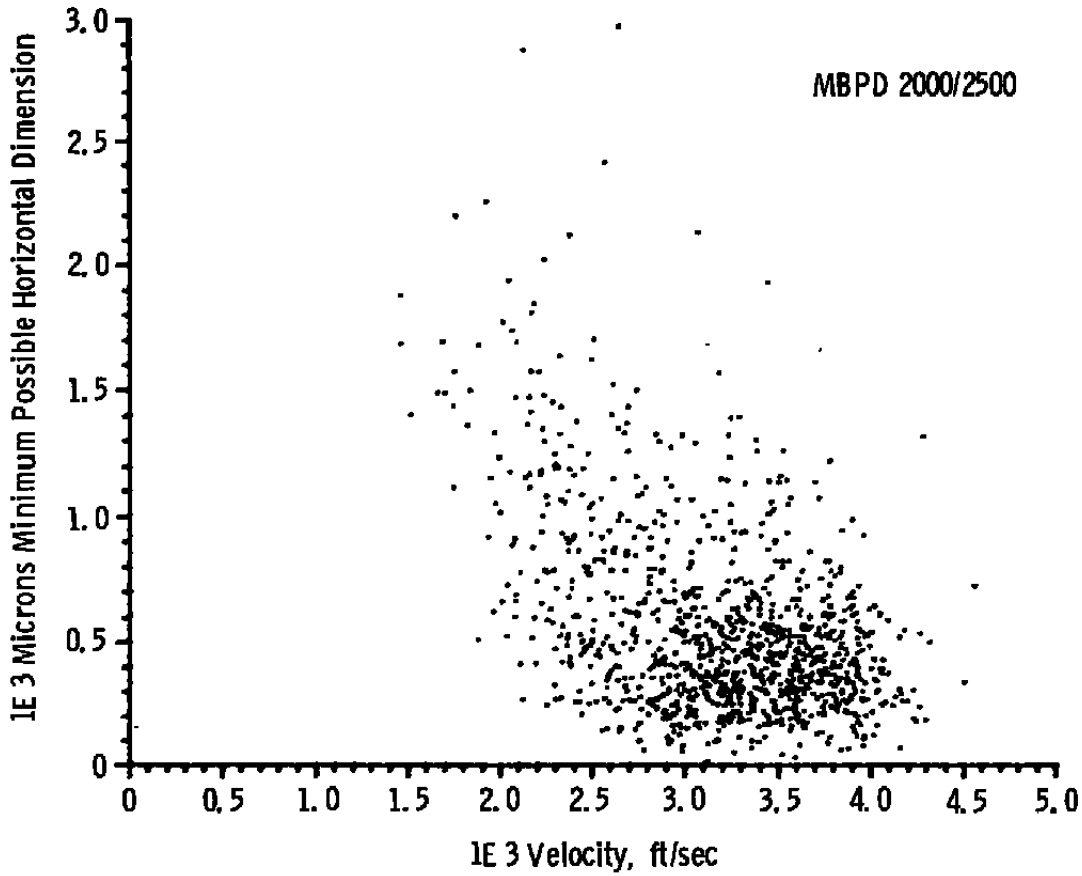

Figure 33. Minimum possible horizontal size versus horizontal velocity.

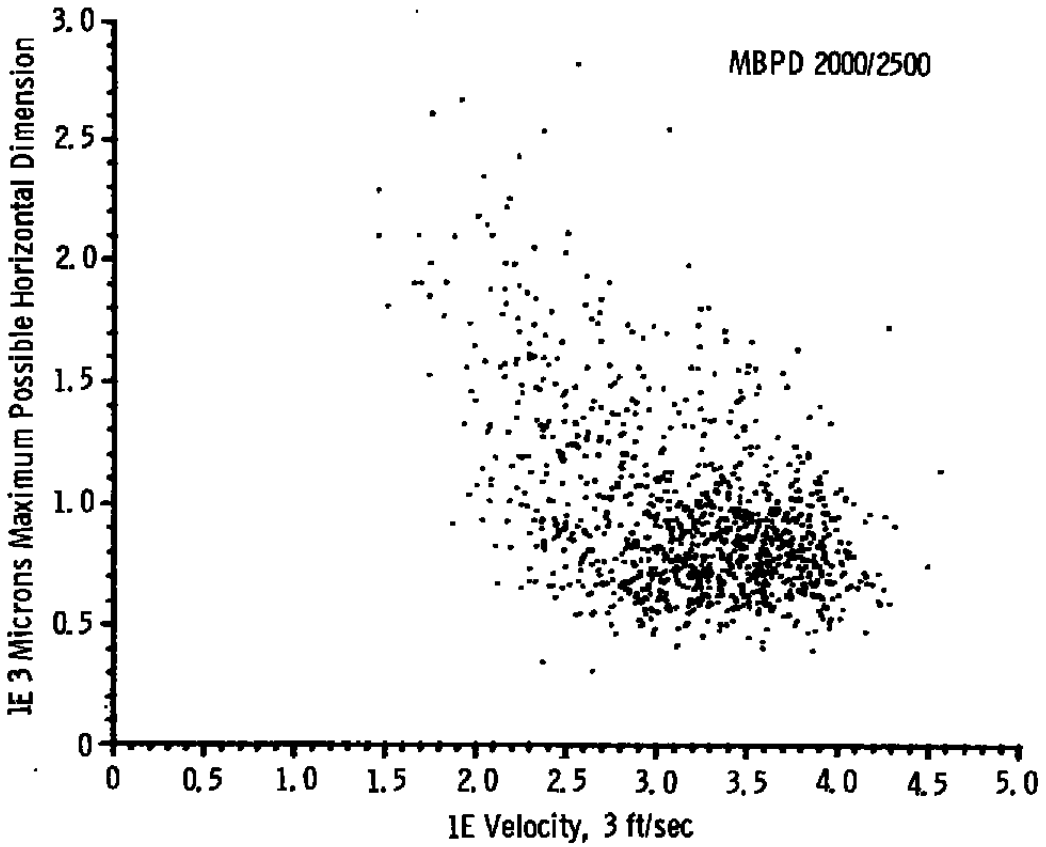

Figure 34. Maximum possible horizontal size versus horizontal velocity.

Trends are evident in the data that the multibeam system performed correctly and that much of the data is reasonably accurate. Particle horizontal dimension was measured by a time-of-flight technique which is fundamentally different from the pulse-height analysis technique (V/V_{max} data attributable to a particle vertical dimension blocking the ribbon beam). These two types of data correlate well, and both indicate that many of the injected particles break up into smaller particles at both the 650-μm and the 2,000-μm mean injected particle sizes. There is no evidence in the data that consistently supports that a lack of large-size particle data is attributable to an inability of the system to measure large particles, as the 2,000/2,500 (2,000 μm) data show a system capability to measure 650-μm, and therefore a lack of 650-μm sizes for the 650/1,622 data (of 650-μm mean particle size) is not suggestive of a systematic error. Second, there are positive correlations between particle size and inverse velocity, $1/v_p$. The large scatter of data on the latter plots is attributable to the highly irregular particle shape.

Particle size and velocity data from the DET tunnel have also been recorded for the 0.65-mm mean particle size using laser holography. This data also indicate that substantial breakup of the particles occurs, as a 280-μm mean particle size was measured.

6.6 CONCLUDING REMARKS

In summary, a prototype multilaser beam, particle diagnostics system has been described that is capable of simultaneously measuring, with reasonable accuracy, the following parameters of an in-flight particle: (1) horizontal velocity component, (2) horizontal and vertical dimensions, and (3) the relative contribution of an incremental range of particle size to rate per unit area. The design and application of such a system to the DET at AEDC contributed in part to the following system characteristics. For a particle to be accurately detected, (1) it must be either optically opaque (not transparent to light) or of highly irregular geometry, (2) it must be nominally between minimum and maximum dimensions of 0.20 to 2.0 mm respectively, and (3) the number density of particles above the minimum detectable size of 0.2 mm must be low (below approximately 0.3 cm^{-3}). Preliminary performance testing in the DET tunnel indicated that the basic components of the system functioned correctly and reliably. Preliminary data results from DET indicate that the mean particle size ultimately achieved in the DET flow field is smaller than that injected. The data support the previously obtained conclusion that breakup of particles occurs during injection and acceleration.

7.0 SUMMARY

Three newly developed laser electro-optical systems capable of extracting certain diagnostic information from in-flight particle clouds in the arc-heated, particle-injected

ablation/erosion facilities at the AEDC have been discussed. One system, the thermal emission velocimeter (TEV), was based on photodetecting the thermal emission radiated by the particles to measure local particle velocity. This system was applied to the (particle-injected) High Enthalpy Ablation Testing (HEAT) facility and now is a routinely used, reliable, and highly accurate diagnostic tool. The other two particle diagnostic systems were developed and applied to the Dust Erosion Tunnel (DET). Both rely on photodetecting the pulses in transmitted beam power caused by particles intercepting one or more spatially separated, separately photodetected laser beams. The particle rate monitor employs a single laser beam to monitor local changes in rate per unit area of the dust cloud. This system has also been developed to a stage such that it now performs reliably and requires, much of the time, only routine operation. The laser multibeam particle diagnostic system was, at the time of writing, in an early development stage; however, proof-of-principle measurements had been made using a prototype system in the DET tunnel. These measurements demonstrated that such a system can be used to measure simultaneously the following parameters of individual, in-flight particles: two-orthogonal dimension of size, one component of velocity and information relating to the local, relative rate per unit area.

REFERENCES

1. Belz, R. A. and Menzel, R. W. "Particle Field Holography at Arnold Engineering Development Center." *Optical Engineering*, Vol. 18, No. 3, May-June 1979.

2. Brayton, D. B. "Velocimetry of Hot Particles by Detection of Thermal Emission," presented at the 25th International Instrumentation Symposium on Aerospace Test Measurements, sponsored by the Instrument Society of America, Anaheim, CA, May 7-10, 1979. (Paper did not appear in the published proceedings; however, copies were made available to those who attended).

3. Trolinger, J. D. and Belz, R. A. "Holography in Dust Erosion Facilities." AEDC-TR-73-160 (AD766420), September 1973.

4. Cline, V. A., Jr. "Dust Particle Velocity Measurements Using a Laser Velocimeter." AEDC-TR-72-159 (AD752225), December 1972.

5. Bentley, H. T., III. "Fiber Optics Particle Sizing System." AEDC-TR-73-111 (AD766647), September 1973.

6. Lewis, H. F., et al. "Description and Calibration Results of the AEDC Dust Erosion Tunnel." AEDC-TR-73-74 (AD910291L), May 1973.

7. *Photomultiplier Manual, Theory, Design, Application,* Technical Series PT-61, RCA Corporation, Harrison, NJ, September 1970, pp. 56-76.

APPENDIX A
BLACKBODY THERMAL EMISSION AND TEV SIGNAL

The characteristics of the thermal radiation emitted by a blackbody will be briefly outlined. The results will be applied in this appendix and the main text to define the thermal signal and thermal noise components, respectively.

Thermally emitted blackbody radiation is characterized by a Lambertian or cosine distribution of power versus angle between the radiation direction and the surface normal, i.e.,

$$N'_\lambda = N_\lambda \cos\beta \tag{A-1}$$

where β is the angle between the radiation N'_λ and the surface normal (power • area^{-1} • wavelength^{-1} • solid angle^{-1}, or w • m^{-3} • sr^{-1}) is the monochromatic thermal radiation intensity in the normal direction, given by Planck's law

$$N_\lambda = C_1 \lambda^{-5} \left(\exp \frac{C_2}{\lambda T} - 1\right)^{-1} \tag{A-2}$$

where T (°K) is the absolute temperature, λ (cm) the monochromatic wavelength, $C_1 = 1.190 \times 10^{-12}$ w • cm^2, and $C_2 = 1.439$ cm • °K. Eq. (A-2) is plotted in Fig. A-1.

With the aid of Eq. (A-1) it can be shown that a small radiating elemental area observed at an oblique angle β is equivalent to a reduced (by a factor cos β) projected area emitting along its surface normal. Therefore, for example, a small spherical blackbody (for example, a TEV thermal particle) will radiate as if it were a blackbody disk of the same diameter as the sphere and with the normal-to-the-disk surface parallel to the observation direction.

For a particle in the high radiation collection efficiency region of a probe volume (see Appendix B), the thermal signal power incident on the detector is given by, assuming $D_p \leq D_v$ (see Fig. A-2),

$$P_p = \Omega_c A_p \int_0^\infty \alpha_p N_\lambda(T_p)\, d\lambda \equiv \Omega_c A_p \int_{\lambda_1}^{\lambda_2} \alpha_p N_\lambda(T_p)\, d\lambda \equiv \Omega_c A_p \bar{\alpha}_p \bar{N}_\lambda(T_p) \Delta\lambda \tag{A-3}$$

where $\Omega_c = \pi\theta_c^2/4$ is the solid collection angle of the detector optics, A_p is the cross section or projected area of radiation of the particle ($A_p = \pi D_p^2/4$ for a spherical particle), α_p is the particle emissivity, $N_\lambda(T_p)$ is the particle monochromatic thermal radiation intensity in the normal direction, λ_1 and λ_2 ($\lambda_2 > \lambda_1$) are the wavelengths at which the overall detection

efficiency (or product of detector quantum efficiency and optical system transmission coefficient) of the TEV drops below 50 percent, $\Delta\lambda = \lambda_2 - \lambda_1$, and the raised bar notation denotes average value over the wavelength interval $\Delta\lambda = \lambda_2 - \lambda_1$.

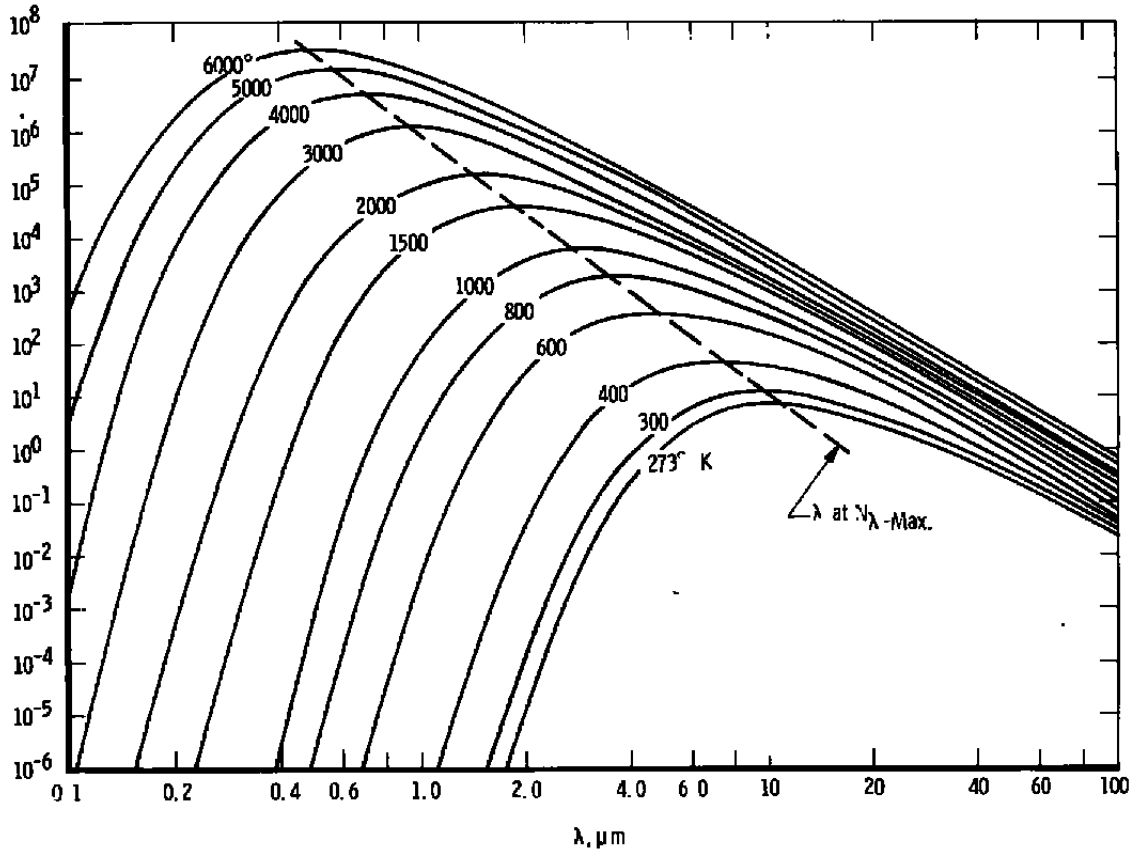

Figure A-1. Normal component of spectral radiant intensity, N_λ, (watt . m^{-2} . sr^{-1} . μm^{-1}) for a blackbody as a function of temperature and wavelength.

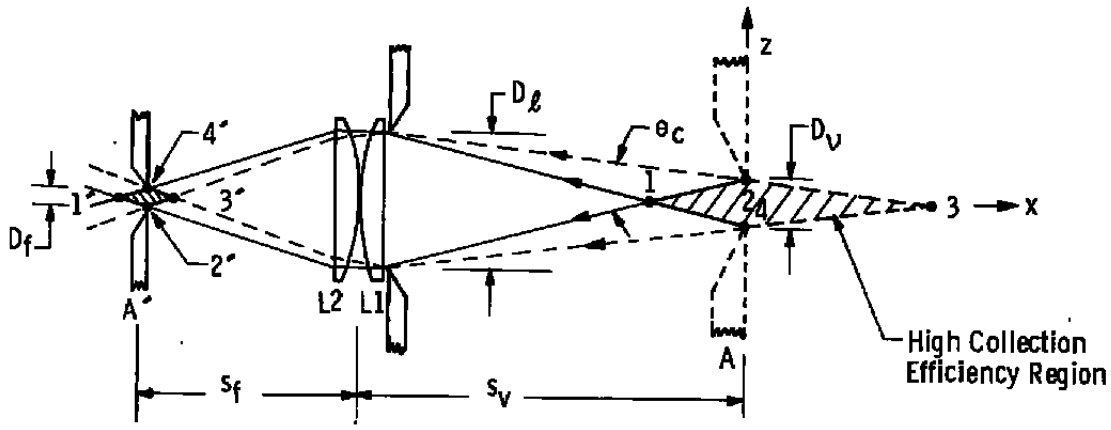

Figure A-2. Aperture lens-pair radiation collection diagram.

APPENDIX B
RADIATION COLLECTION EFFICIENCY

The purpose of this appendix is to review very briefly the radiation collection efficiency of an imaging lens pair followed by a circular transmission aperture such as a fiber-optic component.

The optical system to be discussed is shown in Fig. A-2. A pair of positive lenses, of the achromatic point source collimating type, will be used to represent a simple form of a general type of high spatial resolution, achromatic imaging system. Assume that points 1, 2, 3, and 4 to the right of the imaging lenses are point sources of light; these will image then to points 1′, 2′, 3′, and 4′ to the left of the lenses such that all of the infinity of rays from point 2, for example, that intercept the aperture of lens L1 will be directed by the lenses to pass through point 2. Ray traces such as these can be employed to show the following: (1) points within the shaded region 1, 2, 3, 4 image to points within the shaded region 1′, 2′, 3′, 4′ such that the former region is a region of high (point source) radiation collection efficiency, so high, in fact, that all rays from a point within this region that also intercept the aperture of lens L1 will pass through aperture A and be collected; (2) any ray, directed from

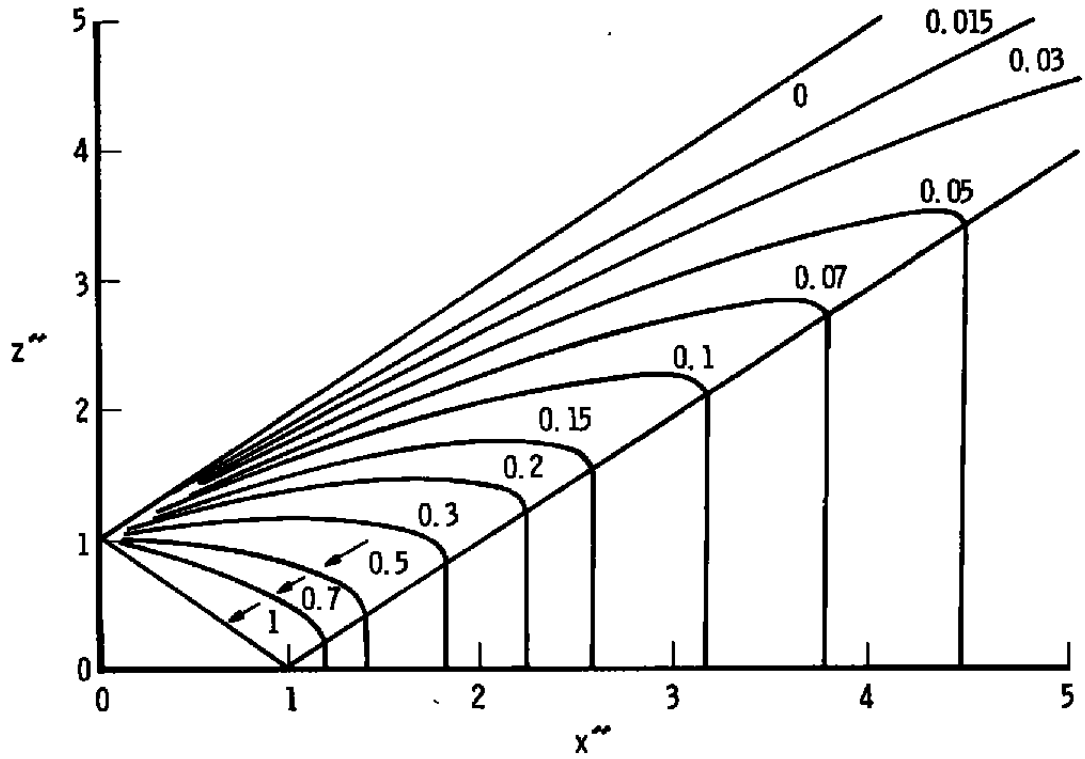

Figure B-1. Contour plot of the relative radiation collection efficiency for the optical system of Fig. A-2.

right to left that is inline with the virtual hole in the virtual aperture A and the aperture of lens L1 will be redirected by the lenses to pass through the real aperture A′ and be collected; any right-to-left ray that does not meet these criteria will intercept the opaque (non-hole) portion of aperture A′ and therefore will not be collected.

A thorough understanding of these statements, in conjunction with elementary ray tracing techniques, will permit computation of surfaces of constant radiation collection efficiency for the region to the right of the lenses. One quandrant of a contour diagram formed by the intersection of such surfaces with the x-z plane is shown in Fig. B-1. The values of Fig. B-1 were computed assuming the employment of circular (x-axis symmetric) optical components and assuming $s_v >> D_\ell >> D_v$, which is typical of many geometries. The coordinates of Fig. B-1 are normalized such that

$$x'' = \frac{D_\ell}{D_v s_v} x \quad \text{and} \quad z'' = \frac{2}{D_v} z \tag{B-1}$$

For $s_v >> D_\ell >> D_v$ the contours of constant collection efficiency are symmetric also about the z-axis, and therefore all four quandrants would plot identically. The relative radiation collection efficiency, Ω_c', plotted in Fig. B-1 is related to the actual, effective radiation collection solid angle, Ω_c, by

$$\Omega_c' = \frac{4 s_v^2}{\pi D_\ell^2} \Omega_c \tag{B-2}$$

again assuming $s_v >> D_\ell >> D_v$.

APPENDIX C
INHERENT SIGNAL-TO-NOISE RATIO (SNR)

Because of the statistical nature of the number of photons detected during the passage of a thermal particle through a TEV probe volume, for example, the TEV signal amplitude is inherently uncertain and noisy. The relative magnitude of such inherent noise will now be discussed.

For the TEV, the photon flux impinging on the PMT photocathode originates from a thermal broadband source and the photons can be assumed to be emitted at random time intervals. Under such conditions the probability that n photons will strike the photocathode in a time interval τ is given by a Poisson distribution (Ref. 7) as follows:

$$P_{(n,\tau)} = \frac{(\overset{o}{N}_{ph}\,\tau)^n}{n!} \exp(-\overset{o}{N}_{ph}\,\tau) \tag{C-1}$$

where N_{ph} is the average photon arrival rate. The average value for n and the variance in n, σ^2_{ph}, can be obtained directly from $P(n,\tau)$ (Ref. 7) as

$$\bar{n} = \overset{o}{N}_{ph}\,\tau \tag{C-2}$$

$$\sigma^2_{ph} = \overset{o}{N}_{ph}\,\tau = \bar{n} \tag{C-3}$$

The inherent photon flux signal-to-noise ratio, $\bar{r}_{ph}$, is given by

$$SNR_{ph} = (\overset{o}{N}_{ph}\,\tau)^{1/2} \tag{C-4}$$

and the inherent cathode photoelectron SNR for a single TEV particle pulse is given by

$$SNR = (\eta\,\overset{o}{N}_{ph}\,\tau)^{1/2} = (\beta p_p\,\tau)^{1/2} = \left[\beta N_\lambda(T_p)\,\alpha_p A_p \Omega_c \lambda\lambda\,(D_p + D_v)\,v_p^{-1}\right]^{1/2} \tag{C-5}$$

The various parameters of Eq. (C-5) are defined in the Nomenclature. The time duration of the TEV signal pulse is $\tau = (D_p + D_v)v_p^{-1}$.

The amplification or multiplication of the cathode photoelectron current in the PMT dynode chain is essentially noise-free. The use of a high-gain PMT in conjunction with a

low-pass filter of bandwidth $\tau^{-1} = (D_p + D_v)^{-1} v_p$ and a low-noise amplifier (if necessary)* ensures that the cathode photoelectron SNR is preserved to within a factor of two at the filter or amplifier output. During the occurrence of the signal pulse (with the particle approximately centered in the probe volume for SNR $>>$ 1), the filter or amplifier output voltage level will achieve a mean peak value and an average variance of the peak that provides a voltage ratio SNR that is within a factor of two of the charge ratio SNR that appeared in the PMT cathode and plate electron currents. Thus, the quantum nature of the photon flux from a detected TEV particle causes an inherent photon flux SNR; this SNR is then reduced by a factor η upon photodetection and then approximately preserved through the electron multiplication, electronic amplification, and low-pass filtering processes.

*A signal amplifier is usually necessary with low photoelectron SNR (SNR $<$ 10) depending on the input voltage level requirements of the signal processor.

APPENDIX D
PARTICLE RATE MONITOR OPTICS

The particle rate monitor optical system that generated and detected the cone beam is shown in Fig. D-1. A 0.005-w helium-neon laser source (S) of 0.6328-μm wavelength, emitted a TEM_{00} approximately collimated, continuous-wave laser beam of nominally 0.6-mm diameter. The laser illuminated, by way of lens L1, a piece of light-diffusing tape, D. The diffusing tape was Scotch® tape No. 810, the commonly used office type that could be written upon. The tape scattered and absorbed all of the incident light, with approximately 0.4 percent (20 μw) scattered into a principal low-divergence, forward-scatter cone of approximately θ = 0.2-radian divergence angle. This then intercepted a 100-μm-diam, centered circular aperture A1. It should be noted that the lens L1 focused the Gaussian laser beam to a spot diameter that was smaller than the aperture A1 (to the focus point (2) of Fig. D-1), and that the distance between L1 and the diffuser-aperture (D-A1) combination was varied so that the aperture diameter was fully illuminated with approximately 40 percent of the power scattered forward in the principal lobe intercepting the aperture A1. The aperture A1, in conjunction with the very closely located diffuser tape D, effectively created a disk of point sources that was imaged by way of lens L2 and aperture A2 (which controlled the cone convergence-divergence angle), out into the test section at position (3) to a 500-μm disk (of focused or imaged point sources). Lens L3 reimaged the cone beam onto a photomultiplier tube. Aperture A3 and the laser line (spectral) filter LLF were employed to reject radiation from test cell camera lights.

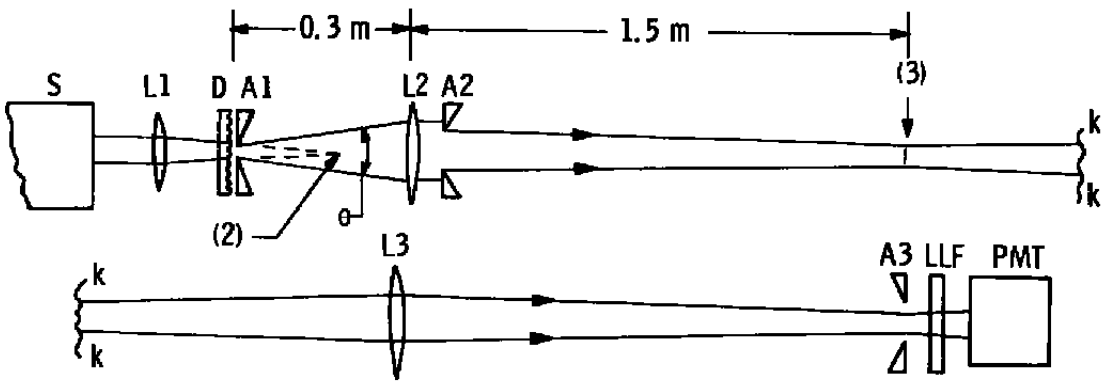

Figure D-1. Particle rate monitor optics.

APPENDIX E
RADIAL INTENSITY VARIATION OF A TRUNCATED CONE BEAM

The particle rate monitor system discussed in the main text followed the assumption that within the truncated cone beam boundaries the beam intensity varied in the axial direction but not in the radial direction. This assumption, however, is not strictly correct. Nevertheless, it serves well as a simplified model to explain the operating principles of the particle RM system. In this appendix it is noted that the actual intensity distribution does indeed vary in the radial direction, especially in the region just adjacent to the disk focus. Why this variation would not affect the relative output of the rate monitor system is discussed here, as well as the type of measurement for which a correct cone beam model would be of concern.

The data of Fig. E-1 were obtained by considering the true (actual) intensity distribution of a particular cone beam geometry. Note that the contours of constant intensity are not straight lines (corresponding to the intersection of a cone surface with a plane through its axis) in regions just adjacent to the disk focus (disk real image). However, for more remote regions they do become straight. Data are provided on Fig. E-1 that locate the two regions in which the radial intensity variation is highly nonuniform; these regions are symmetrically displaced about the plane of the disk focus.

The radial intensity variation of the truncated cone beam will not affect the RM system relative data (local relative particle rate per unit area versus time) provided that each of the following two particle field parameters varies independently of the mass injection rate (mass • time^{-1}) of particle material: (1) the relative size distribution of particles in the measurement region (counts per unit increment of size versus size divided by total counts from all sizes) and (2) the geometrical distribution of relative particle flux (local number • time^{-1} • area^{-1} divided by spatially averaged value of same). These two requirements appear to be reasonably met for the DET application; thus, the RM relative data versus time would be independent of the exact radial and/or axial intensity distribution of the truncated cone beam that was employed.

Variation of either the intensity distribution or of the beam power trigger level of the truncated cone beam will affect the detection cross section of the system for any particle size. As discussed earlier and in the text, such variations will not change the *relative* system performance. Such variations will, however, alter any nonrelative, quantitative count data that is proportional to or varies as a function of detection cross section. Thus, for example, had allowances not been made for the decreasing power of the truncated cone beam (because

of window contamination during a run) by providing relative or proportional trigger level circuitry (see main text), then the RM detection cross section would vary during a run; the latter would cause the apparent data rate to vary and be in error.

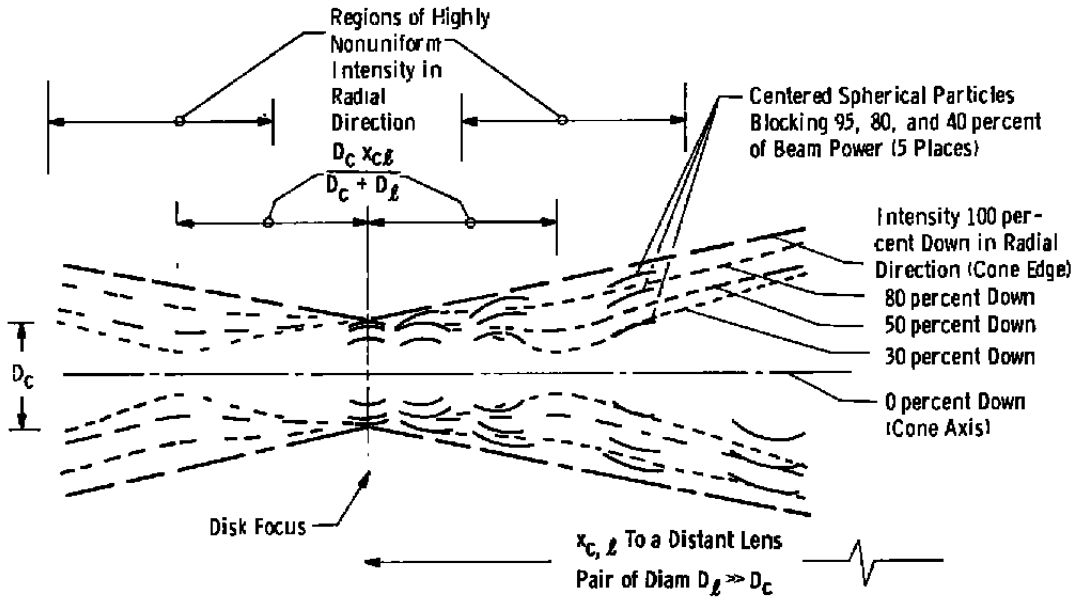

Figure E-1. Intensity variation in the radial direction near the focus of a truncated cone beam.

APPENDIX F
MULTIBEAM ILLUMINATING OPTICS

A more detailed description of the performance of the multibeam system's illuminating electro-optical package will now be presented.

The mirrors contained within the multibeam illiminating package (Fig. 16) folded the optical path so that the optics could be contained in a relatively compact package. The 1.0-mm-diam, 1-mw TEM_{oo} laser output beam intercepted a 100-mm focal length (F.L.) lens which focused the beam onto a 0.20-mm-diam pinhole. The beam was spatial filtered to remove extraneous diffraction patterns from its intensity distribution, and then expanded to 0.6 mm diameter, where it was recollimated by a 60-mm F.L. lens. Two 45-deg glass prisms expanded the beam only in one dimension (y-axis) to an elliptical cross section of 0.6 mm by 6.0 mm. This collimated beam was then split into two similar, approximately parallel beams which illuminated the pencil-disk-ribbon hole pattern of Fig. 17 machined into a 0.1-mm-thick metal mask, thereby generating the four mulitple beams. The diffracted output radiation, still containing a large fraction of its energy in a collimated wavefront form, was then focused by a 500-mm lens to within a very small spot (to the small size of the Fraunhofer diffraction pattern of the aperture mask), allowed to reexpand to its original dimensions of beam centerline spacings, and then reimaged to a point 1 m away by a 50-mm lens that simultaneously recollimated the four beam centerlines. In this way the illuminating optics provided a projected real image, with unity (1:1) magnification, of the four transmission holes in the aperture mask such that centerlines of each of the four imaging bundles of radiation were collimated or parallel to one another.

NOMENCLATURE

A	Aperture mask
A_p	Cross-sectional area of particle; $\pi D_p^2/4$ for a spherical particle, m^2
$\overline{A_p}$	Mean or average value of A_p, m^2
ASA	American Standard speed (or exposure index) of a photographic emulsion
A_v	Probe-volume virtual-aperture area or maximum cross-sectional area of the high-detectivity region of the probe volume, m^2
BE	Beam expander
BE(JD)	J-dimensional beam expander
BS	Beamsplitter
bit	Binary number (0 or 1)
byte	Eight bits
c.t.c.	Center to center
2D	Two dimensional
Dc	(Minimum) diameter of cone-beam (Fig. 10), m
Dc,max	Maximum diameter of cone-beam at P.F. edge, m
D_f	Diameter of optical fiber, m
D_f	Diameter of lens or lens system aperture, m
D_p	Diameter of particle, m
D_{pf}	Diameter of particle field (Fig. 10), m
D_v	Diameter of the probe volume virtual aperture or diameter of the high-detection region of the probe volume, m
f	Lens focal length in mm
F	Depth-of-field distance (or length of collimated beam region), m

F_c	Depth-of-field of cone beam (Fig. 10), m
F_r	Depth-of-field of ribbon beam (Fig. 10), m
Δf	Electronic bandwidth, Hz
GPIB	General purpose interface bus
HEAT	High enthalpy ablation testing
k	Kilo or 1,000
L	He-Ne laser
LV	Laser velocimeter
L_v	Effective probe volume length dimension, m
M	Mirror
micron	Micrometer or 10^{-6} meter
MBPD	Multibeam particle diagnostic
N_p	Total number of particles in the particle field
$\dot{N}_{ph}$	Average or mean photon arrival rate, Hz
N_λ, $N_\lambda(T)$	Spectral radiant intensity in the normal direction ($w \cdot m^{-3} \cdot sr^{-1}$)
$\overline{N_\lambda}(T)$	Value of $N_\lambda(T)$ averaged over the wavelength interval $\Delta\lambda = \lambda_2 - \lambda_1$ ($w \cdot m^{-3} \cdot sr$)
N'_λ	Spectral radiant intensity at an angle β relative to the surface normal, ($w \cdot m^{-3} \cdot sr^{-1}$)
n	Number of photons received over some time interval; number of photocathode electron events detected as one thermal particle pases through one probe volume
$\bar{n}$	Average or mean value of n
n_p	Number of particles per unit volume, m^{-3}

P.F.	Particle field
PH	Pinhole
PMT	Photomultiplier tube
$P_{(n,\tau)}$	Probability of n events over a time period τ with a Poisson distribution
p	Total cone beam power, w
p_b	Power radiated by the backdrop (background surface) inline with both the virtual aperture and the aperture of the collecting lens system (to be collected and detected, w
p_p	Power radiated by the particle that is incident onto the detector, w
RM	Rate monitor
SNR	Inherent signal-to-noise ratio of the photoelectron signal burst generated by a single particle
SNR_{ph}	Inherent signal-to-noise ratio of the collected photon signal burst from a single particle
s_f	Distance of object (fiber optic) from imaging lens system, m
s_v	Distance of probe volume from imaging lens system, m
T	Absolute temperature, °K
TEM_{oo}	Propagating electromagnetic wave with transverse electric and magnetic (TEM) fields and Gaussian intensity distribution
TEV	Thermal emission velocimeter
V	Signal voltage reduction of ribbon beam (Fig. 12), v
V_{max}	Maximum V (due to beam extinction) (Fig. 12), v
V_p	Particle z velocity components, $msec^{-1}$
V1, V_1	Upstream probe volume region
V2, V_2	Downstream probe volume region

V_v	Volume of the principal or high collection efficiency region of the probe volume assuming $s_v >> D_f >> D_v$; detection volume or volume within which a particle must be to be detected, m^3
v_p	Velocity of particle, $(m \cdot s^{-1})$
x	Displacement coordinate axis parallel to laser-beam centerlines (multibeam) or collection-lens axis (TEV), m; x-axis position of particle, m
x,y,z	Coordinate system with x-axis parallel to the optical direction and with z-axis parallel to the flow direction
x_{pf}	X-axis or depth dimension of particle field, m
x_{vb}	Distance between the probe volume and the backdrop surface, m
x''	Normalized x-axis coordinate of a single probe volume region coordinate system
y	Vertical displacement coordinate orthogonal to both the flow direction (horizontal or z-axis) and the mean optical propagation direction (x-axis), m; y-axis position of particle, m
y_p	Particle y-axis (vertical) dimension (size), m
y_{pc}	Y distance between cone and pencil beam centerlines (Fig. 10), m
y_{pp}	Y distance between pencil beams (Fig. 10), m
y_r	Y or vertical dimension of ribbon beam (Fig. 10), m
z	Horizontal displacement coordinate axis parallel to flow direction, m; z-axis position of particle, m
Z_{cr}	Z-axis distance between cone and ribbon beams (Fig. 10), m
Z_p	Particle Z-axis dimension (Fig. 12), m
Z_{pc}	Z-axis distance between pencil and cone beams (Fig. 10), m
$Z_{p,min}$	Minimum particle z dimension, m
$Z_{p,max}$	Maximum particle z dimension, m

Z_r, $Z_r(x)$	Z dimension of ribbon beam (a function of x), m
$Z_{r,min}$	Minimum z dimension of ribbon beam (Fig. 10), m
$Z_{r,max}$	Maximum z dimension of ribbon beam (Fig. 10), m
ZCD	Zero-crossing detector
Δz, Δz_v	Particle displacement distance corresponding to duration of TEV signal for one probe volume, m; z-axis probe volume dimension, m
z''	Normalized z-axis coordinate of a single probe volume region coordinate system
z_{12}	Z-axis distance between the upstream and the downstream probe volume, m
α_b	Emissivity of backdrop surface
$(1 - \alpha_b)$	Diffuse reflection coefficient of backdrop surface
α_p	Emissivity of particle
$\bar{\alpha}_p$	Detection-interval ($\Delta\lambda$)-averaged α_p
β	PMT cathode photoelectron yield per joule of incident energy, (j^{-1})
γ	Relative value of the beam power trigger level setting (of maximum value 1)
η	Quantum efficiency (photocathode electrons per photon)
θ	Divergence angle of radiation cone of Fig. 13, r
$\theta_{1,2}$	Angle between the probe volume axes, r
θ_c	Angle of radiation collection; same as θ_v, r; divergence angle of cone beam, r (Fig. 10)
θ_r	Divergence angle of ribbon beam (Fig. 10), r
θ_v	Angle of a probe volume high-detectivity region; same as θ_c, r
λ	Wavelength of thermal emission, m
$\Delta\lambda = \lambda_2 - \lambda_1$	Wavelength band for which detection efficiency is 50 percent or greater, m

λ_1	Lower wavelength limit for which detection efficiency is 50 percent or greater, m
λ_2	Upper wavelength limit for which detection efficiency is 50 percent or greater, m
$\lambda_{T\text{-}MAX}$	Wavelength corresponding to the peak (maximum) value of $N_\lambda(T)$, m
σ	Detection cross section or detection area, m^2
σ_{ph}^2	Variance in n
τ	Signal period; time period, s
τ_1	Time between occurrences of auxiliary-circuit signal pulse and ribbon-beam signal pulse (Fig. 12), s
τ_2	Time duration of ribbon-beam signal pulse (Fig. 12), s
Ω_c	Solid angle of radiation collection; $\pi\theta_c^2/4$, sr
Q_c'	Relative radiation collection efficiency (of maximum value 1)
650/1,622, etc.	650-μm particle size/1,622-μm y-dimension of ribbon beam, $\mu m/\mu m$